PHYSICAL REVIEW D **86,** 024011 (2012)

Prototype effective-one-body model for nonprecessing spinning inspiral-merger-ringdown waveforms

Andrea Taracchini,[1] Yi Pan,[1] Alessandra Buonanno,[1,2] Enrico Barausse,[3,1] Michael Boyle,[4] Tony Chu,[5] Geoffrey Lovelace,[4] Harald P. Pfeiffer,[5] and Mark A. Scheel[6]

[1]*Maryland Center for Fundamental Physics and Joint Space-Science Institute, Department of Physics, University of Maryland, College Park, Maryland 20742, USA*

[2]*Radcliffe Institute for Advanced Study, Harvard University, 8 Garden Street, Cambridge, Massachusetts 02138, USA*

[3]*Department of Physics, University of Guelph, Guelph, Ontario N1G 2W1, Canada*

[4]*Center for Radiophysics and Space Research, Cornell University, Ithaca, New York, 14853, USA*

[5]*Canadian Institute for Theoretical Astrophysics, 60 St. George Street, University of Toronto, Toronto, Ontario M5S 3H8, Canada*

[6]*Theoretical Astrophysics 350-17, California Institute of Technology, Pasadena, California 91125, USA*

(Received 17 February 2012; published 5 July 2012)

This paper presents a tunable effective-one-body (EOB) model for black-hole (BH) binaries of arbitrary mass ratio and aligned spins. This new EOB model incorporates recent results of small-mass-ratio simulations based on Teukolsky's perturbative formalism. The free parameters of the model are calibrated to numerical-relativity simulations of nonspinning BH-BH systems of five different mass ratios and to equal-mass nonprecessing BH-BH systems with dimensionless BH spins $\chi_i \simeq \pm 0.44$. The present analysis focuses on the orbital dynamics of the resulting EOB model, and on the dominant $(\ell, m) = (2, 2)$ gravitational-wave mode. The calibrated EOB model can generate inspiral-merger-ringdown waveforms for nonprecessing, spinning BH binaries with any mass ratio and with individual BH spins $-1 \leq \chi_i \lesssim 0.7$. Extremizing only over time and phase shifts, the calibrated EOB model has overlaps larger than 0.997 with each of the seven numerical-relativity waveforms for total masses between $20M_\odot$ and $200M_\odot$, using the Advanced LIGO noise curve. We compare the calibrated EOB model with two additional equal-mass highly spinning ($\chi_i \simeq -0.95, +0.97$) numerical-relativity waveforms, which were not used during calibration. We find that the calibrated model has an overlap larger than 0.995 with the simulation with nearly extremal *antialigned* spins. Extension of this model to black holes with *aligned* spins $\chi_i \gtrsim 0.7$ requires improvements of our modeling of the plunge dynamics and inclusion of higher-order PN spin terms in the gravitational-wave modes and radiation-reaction force.

DOI: 10.1103/PhysRevD.86.024011 PACS numbers: 04.25.D−, 04.25.dg, 04.25.Nx, 04.30.−w

I. INTRODUCTION

Coalescing compact-object binary systems (binaries, for short) are among the most promising sources of gravitational waves (GWs) for detectors like the U.S. Laser Interferometer Gravitational-Wave Observatory (LIGO), the British-German GEO, and the French-Italian Virgo [1–3]. LIGO and Virgo are undergoing upgrades to Advanced configurations [4], which will improve sensitivity by about a factor of 10. A detailed and accurate understanding of the GWs radiated as the bodies in a binary spiral towards each other is crucial not only for the initial detection of such sources, but also for maximizing the information that can be obtained from the GW signals once they are observed.

The matched-filtering technique is the primary data-analysis tool used to extract the GW signals from the detectors' noise. It requires accurate waveform models of the expected GW signals. Analytical templates based on the post-Newtonian (PN) approximation [5–8] of the Einstein field equations developed over the past 30 years accurately describe the inspiraling stage of the binary evolution. In 1999 a new approach to the two-body dynamics of compact objects, the so-called effective-one-body (EOB) approach, was proposed with the goal of extending the analytical templates throughout the last stages of inspiral, plunge, merger, and ringdown. The EOB approach uses the results of PN theory, black-hole perturbation theory, and, more recently, the gravitational self-force formalism. It does not, however, use the PN results in their original Taylor-expanded form (i.e., as polynomials in v/c), but in a resummed form.

The EOB formalism was first proposed in Refs. [9,10] and subsequently improved in Refs. [11–13]. Using physical intuition and results from black-hole perturbation theory and the close-limit approximation, Refs. [10,13] computed preliminary plunge, merger, and ringdown signals of nonspinning and spinning black-hole binaries. After breakthroughs in numerical relativity (NR) [14–16], the EOB inspiral-merger-ringdown waveforms were improved by calibrating the model to progressively more accurate NR simulations, spanning larger regions of the parameter space [17–27]. More recently, an EOB model for the dominant (2, 2) mode and four subdominant modes was built for nonspinning binaries of comparable masses [27] and the small-mass-ratio limit [28]. These results, at the interface between numerical and analytical relativity, have already had an impact in LIGO and Virgo searches. The

first searches of high-mass and intermediate-mass black-hole binaries in LIGO/Virgo data [29,30] used the inspiral-merger-ringdown templates generated by the EOB model calibrated in Ref. [19], as well as the phenomenological templates proposed in Ref. [31].

Stellar-mass black holes are expected to carry spins, which significantly increases the dimension of the binary parameter space. The first EOB Hamiltonian with leading-order (1.5PN) spin-orbit and (2PN) spin-spin couplings was developed in Ref. [12]. Then, Ref. [13] worked out the radiation-reaction force in the EOB equations of motion in the presence of spins and computed inspiral-merger-ringdown waveforms for generic spinning binaries, capturing their main features, including the so-called "hang up." Later, Ref. [32] incorporated the next-to-leading-order (2.5PN) spin-orbit couplings in the EOB Hamiltonian. By construction, in the test-particle limit the Hamiltonian of Ref. [32] does not reduce to the Hamiltonian of a spinning test particle in the Kerr spacetime. Moreover, the Hamiltonian of Ref. [32] rewrites the EOB radial potential using Padé summation, causing spurious poles in some regions of parameter space. Nevertheless, the Hamiltonian of Ref. [32] was adopted in Ref. [25] to demonstrate the possibility of calibrating the EOB model for spinning binaries.

Since then, substantial progress has been made towards improving the spin EOB Hamiltonian. Reference [33] worked out the Hamiltonian for a spinning test-particle in a generic spacetime, which was used in Ref. [34] to derive a spin EOB Hamiltonian having the correct test-particle limit. Furthermore, Ref. [34] rewrote the EOB radial potential in a way that guarantees the absence of poles without employing the Padé summation. As a consequence, the EOB Hamiltonian of Ref. [34] has desirable strong-field circular-orbit features, such as the existence of an innermost-stable circular orbit (ISCO), a photon circular orbit (or light-ring), and a maximum in the orbital frequency during the plunge. Still preserving these properties, the spin EOB Hamiltonian of Ref. [34] was recently extended to include the next-to-next-to-leading-order (3.5PN) spin-orbit couplings in Ref. [35]. The EOB Hamiltonian of Ref. [32] was also recently extended through 3.5PN order in the spin-orbit sector in Ref. [36].

In the nonconservative sector of the EOB model, the radiation-reaction force in the EOB equations of motion is built from the GW energy flux, which, in turn, is computed from a decomposition of the waveform into spherical harmonic (ℓ, m) modes. These modes, instead of being used in their Taylor-expanded form, are resummed (or factorized). This factorization was originally proposed in Refs. [37,38] for nonspinning black-hole binaries, and was then extended to include spin effects in Ref. [39] and higher-order PN spinless terms in Refs. [40,41]. In the test-particle limit, the factorized waveforms are known at very high PN order—for example their sum generates the GW energy flux for nonspinning binaries through 14PN [41] order and to 4PN order in terms involving the black-hole spins. However, in the comparable-mass case the GW modes are known only at a much lower PN order. Despite the fact that the GW energy flux in the comparable-mass case is known through 3.5PN [42,43] and 3PN [44] order in the nonspinning and spin-orbit sectors, and 2PN order in the spin-spin sector, the GW modes have been computed only through 1.5PN order for spin-orbit couplings and 2PN order for spin-spin couplings [39,45]. Currently, this lack of information in the GW modes is the main limitation of our spin EOB model, and, as we will see, it affects the performance of the model for prograde orbits and large spin values.

In this paper, we build upon the past success in analytically modeling inspiral-merger-ringdown waveforms through the EOB formalism, and develop a prototype EOB model for nonprecessing spinning black-hole binaries that covers a large region of the parameter space and can be used for detection purposes and future calibrations. More specifically, we adopt the EOB Hamiltonian derived in Refs. [34,35], the GW energy flux and factorized waveforms derived in Refs. [38,39], and calibrate the EOB (2, 2) dominant mode to seven NR waveforms: five nonspinning waveforms with mass ratios 1, 1/2, 1/3, 1/4 and 1/6 [27] and two equal-mass nonprecessing spinning waveforms of spin magnitudes 0.44 [46]. We combine the above results with recent small-mass-ratio results produced by the Teukolsky equation [28] to build a prototype EOB model for inspiral-merger-ringdown waveforms for nonprecessing spinning black-hole binaries with any mass ratio and individual black-hole spins $-1 \leq \chi_i \lesssim 0.7$. For $\chi_i \gtrsim 0.7$, although the EOB dynamics can be evolved until the end of the plunge, the EOB (2, 2) mode peaks too early in the evolution, where the motion is still quasicircular. As a consequence, we cannot correct the EOB (2, 2) mode to agree with the NR (2, 2) mode peak using non-quasicircular amplitude coefficients. This limitation, which also affects the small-mass-ratio limit results [28], is caused by the poor knowledge of PN spin effects in the GW modes and makes the prototype EOB waveforms unreliable for $\chi_i \gtrsim 0.7$. Two NR waveforms with nearly extremal spin magnitudes [47,48] became available to us when we were finishing calibration of the spin EOB model. We use them to examine the limitations of the spin prototype EOB model, and extract from them useful information for future work.

The paper is organized as follows. In Sec. II, we describe the spin EOB model used in this work, its dynamics, waveforms, and adjustable parameters. Section III A discusses the alignment procedure used to compare EOB and NR waveforms at low frequency, and the statistics used to quantify the differences between the waveforms. We then calibrate the EOB model to the NR waveforms in Sec. III B. In Sec. IV, we combine the results of

Sec. III A with those of Ref. [28] to build a prototype EOB model that interpolates between the calibrated EOB waveforms and extends them to a larger region of the parameter space. We also investigate how this prototype EOB model performs with respect to two NR waveforms with nearly extremal spin, which were not used in the calibration. Finally, Sec. V summarizes our main conclusions. In the Appendix we explicitly write the factorized waveforms used in this work, including spin effects.

II. EFFECTIVE-ONE-BODY DYNAMICS AND WAVEFORMS IN THE PRESENCE OF SPIN EFFECTS

In this section, we define the spin EOB model that we will later calibrate using NR waveforms. Henceforth, we use geometric units $G = c = 1$.

In the spin EOB model [12,32,34–36] the dynamics of two black holes of masses m_1 and m_2 and spins $\boldsymbol{S}_1$ and $\boldsymbol{S}_2$ is mapped into the dynamics of an effective particle of mass $\mu = m_1 m_2/(m_1 + m_2)$ and spin $\boldsymbol{S}^*$ moving in a deformed Kerr metric with mass $M = m_1 + m_2$ and spin $\boldsymbol{S}_{\rm Kerr}$. The position and momentum vectors of the effective particle are described by $\boldsymbol{R}$ and $\boldsymbol{P}$, respectively. Here, for convenience, we use the reduced variables

$$\boldsymbol{r} \equiv \frac{\boldsymbol{R}}{M}, \qquad \boldsymbol{p} \equiv \frac{\boldsymbol{P}}{\mu}. \tag{1}$$

Since we will restrict the discussion to spins aligned or antialigned with the orbital angular momentum, we define the (dimensionless) spin variables χ_i as $\boldsymbol{S}_i \equiv \chi_i m_i^2 \hat{\mathbf{L}}$, where $\hat{\mathbf{L}}$ is the unit vector along the direction of the orbital angular momentum. We also write $\boldsymbol{S}_{\rm Kerr} \equiv \chi_{\rm Kerr} M^2 \hat{\mathbf{L}}$.

A. The effective-one-body dynamics

In this paper we adopt the spin EOB Hamiltonian proposed in Refs. [33–35]. The real (or EOB) Hamiltonian is related to the effective Hamiltonian $H_{\rm eff}$ through the relation

$$H_{\rm real} \equiv \mu \hat{H}_{\rm real} = M\sqrt{1 + 2\nu\left(\frac{H_{\rm eff}}{\mu} - 1\right)} - M, \tag{2}$$

where $H_{\rm eff}$ describes the conservative dynamics of an effective spinning particle of mass μ and spin $\boldsymbol{S}^*$ moving in a deformed Kerr spacetime of mass M and spin $\boldsymbol{S}_{\rm Kerr}$. The symmetric mass ratio $\nu = \mu/M$ acts as the deformation parameter. Through 3.5PN order in the spin-orbit coupling, the mapping between the effective and real spin variables reads [34,35]

$$\boldsymbol{S}_{\rm Kerr} = \boldsymbol{S}_1 + \boldsymbol{S}_2, \tag{3a}$$

$$\boldsymbol{S}^* = \frac{m_2}{m_1}\boldsymbol{S}_1 + \frac{m_1}{m_2}\boldsymbol{S}_2 + \boldsymbol{\Delta}^{(1)}_{\sigma^*} + \boldsymbol{\Delta}^{(2)}_{\sigma^*}, \tag{3b}$$

where $\boldsymbol{\Delta}^{(1)}_{\sigma^*}$ and $\boldsymbol{\Delta}^{(2)}_{\sigma^*}$ are the 2.5PN and 3.5PN spin-orbit terms given explicitly in Eqs. (51) and (52) of Ref. [35]. They depend on the dynamical variables $\boldsymbol{r}$ and $\boldsymbol{p}$, the spin variables $\boldsymbol{S}_i$, and on several gauge parameters. These parameters are present because of the large class of canonical transformations that can map between the real and effective descriptions. Their physical effects would cancel out if the PN dynamics were known at arbitrarily high orders; since this is clearly not the case, the gauge parameters can have a noticeable effect [35] and may in principle be used as spin EOB adjustable parameters. In this paper however, we set all gauge parameters to zero and introduce a spin EOB adjustable parameter at 4.5PN order in the spin-orbit sector by adding the following term to Eq. (3b)

$$\boldsymbol{\Delta}^{(3)}_{\sigma^*} = \frac{d_{\rm SO}\nu}{r^3}\left(\frac{m_2}{m_1}\boldsymbol{S}_1 + \frac{m_1}{m_2}\boldsymbol{S}_2\right). \tag{4}$$

Here $d_{\rm SO}$ is the spin-orbit EOB adjustable parameter. The effective Hamiltonian reads [34]

$$\frac{H_{\rm eff}}{\mu} = \beta^i p_i + \alpha\sqrt{1 + \gamma^{ij}p_i p_j + \mathcal{Q}_4(\boldsymbol{p})} + \frac{H_{\rm SO}}{\mu} + \frac{H_{\rm SS}}{\mu} - \frac{1}{2Mr^5}(r^2\delta^{ij} - 3r^i r^j)S^*_i S^*_j, \tag{5}$$

where the first two terms are the Hamiltonian of a nonspinning test particle in the deformed Kerr spacetime, α, β^i and γ^{ij} are the lapse, shift and 3-dimensional metric of the effective geometry and $\mathcal{Q}_4(\boldsymbol{p})$ is a nongeodesic term quartic in the linear momentum introduced in Ref. [49]. The quantities $H_{\rm SO}$ and $H_{\rm SS}$ in Eq. (5) contain, respectively, spin-orbit and spin-spin couplings that are *linear* in the effective particle's spin $\boldsymbol{S}^*$, while the term $-1/(2Mr^5)(r^2\delta^{ij} - 3r^i r^j)S^*_i S^*_j$ is the leading-order coupling of the particle's spin to itself, with δ^{ij} being the Kronecker delta. More explicitly, using Ref. [34] we can obtain $H_{\rm SO}$ and $H_{\rm SS}$ by inserting Eqs. (5.31), (5.32), Eqs. (5.47a)–(5.47h), and Eqs. (5.48)–(5.52) into Eqs. (4.18) and (4.19); α, β^i and γ^{ij} are given by inserting Eqs. (5.36a)–(5.36e), Eqs. (5.38)–(5.40) and Eqs. (5.71)–(5.76) into Eqs. (5.44)–(5.46). We will elucidate our choice of the quartic term $\mathcal{Q}_4(\boldsymbol{p})$ at the end of this section, when introducing the tortoise variables.

Following Ref. [25], we introduce another spin EOB adjustable parameter in the spin-spin sector. Thus, we add to Eq. (5) the following 3PN term

$$\frac{d_{\rm SS}\nu}{r^4}\left(\frac{m_2}{m_1}\boldsymbol{S}_1 + \frac{m_1}{m_2}\boldsymbol{S}_2\right)\cdot(\boldsymbol{S}_1 + \boldsymbol{S}_2), \tag{6}$$

with $d_{\rm SS}$ the spin-spin EOB adjustable parameter. For what concerns the nonspinning EOB sector, we adopt the following choice for the EOB potentials Δ_t and Δ_r entering α, β^i and γ^{ij} (see Eq. (5.36) in Ref. [34]). The potential Δ_t is given through 3PN order by

$$\Delta_t(u) = \frac{1}{u^2}\Delta_u(u), \tag{7a}$$

$$\Delta_u(u) = A(u) + \chi^2_{\rm Kerr}u^2, \tag{7b}$$

$$A(u) = 1 - 2u + 2\nu u^3 + \nu\left(\frac{94}{3} - \frac{41}{32}\pi^2\right)u^4, \tag{7c}$$

where $u \equiv 1/r$. Reference [34] suggested rewriting the quantity $\Delta_u(u)$ as

$$\Delta_u(u) = \bar{\Delta}_u(u)[1 + \nu\Delta_0 + \nu\log(1 + \Delta_1 u + \Delta_2 u^2 + \Delta_3 u^3 + \Delta_4 u^4)], \tag{8}$$

where Δ_i with $i = 1, 2, 3, 4$ are explicitly given in Eqs. (5.77)–(5.81) of Ref. [34], and

$$\bar{\Delta}_u(u) = \chi^2_{\rm Kerr}\left(u - \frac{1}{r^{\rm EOB}_+}\right)\left(u - \frac{1}{r^{\rm EOB}_-}\right), \tag{9a}$$

$$r^{\rm EOB}_\pm = \left(1 \pm \sqrt{1 - \chi^2_{\rm Kerr}}\right)(1 - K\nu). \tag{9b}$$

Here, $r^{\rm EOB}_\pm$ are radii reducing to those of the Kerr event and Cauchy horizons when the EOB adjustable parameter K goes to zero. The logarithm in Eq. (8) was introduced in Ref. [34] to quench the divergence of the powers of u at small radii. Its presence also allows the existence of an ISCO, a photon circular orbit (or light-ring), and a maximum in the orbital frequency during the plunge. The reason for modeling $\Delta_u(u)$ with Eq. (8) instead of using the Padé summation of $\Delta_u(u)$, as proposed in Ref. [32], is threefold. First, we did not want to use the Padé summation of $\Delta_u(u)$ because Ref. [25] found that for certain regions of the parameter space spurious poles can appear. Second, although we could have applied the Padé summation only to $A(u)$ and used the Padé potential $A(u)$ calibrated to nonspinning waveforms in Ref. [27], we want to take advantage of the good properties of the potential (8) during the late inspiral, as found in Ref. [34]. Third, we find it useful to develop a variant of the EOB potential so that in the future we can test how two different EOB potentials (both calibrated to NR waveforms at high frequency) compare at low frequency.

Furthermore, for the potential Δ_r at 3PN order entering the EOB metric components (5.36) in Ref. [34], we choose

$$\Delta_r(u) = \Delta_t(u)D^{-1}(u), \tag{10a}$$

$$D^{-1}(u) = 1 + \log[1 + 6\nu u^2 + 2(26 - 3\nu)\nu u^3]. \tag{10b}$$

Once expanded in PN orders, the EOB Hamiltonian (2) with the effective Hamiltonian defined in Eq. (5) and the spin mapping defined in Eqs. (3a) and (3b), reproduces all known PN orders—at 3PN, 3.5PN and 2PN order in the nonspinning, spin-orbit and spin-spin sectors, respectively—except for the spin-spin terms at 3PN and 4PN order, which have been recently computed in Refs. [50–57]. Furthermore, in the test-particle limit the real Hamiltonian contains the correct spin-orbit couplings linear in the test-particle spin, at *all* PN orders [33,34].

Let $\hat{t} \equiv t/M$. In terms of the reduced Hamiltonian $\hat{H}_{\rm real}$, the EOB Hamilton equations are given in dimensionless form by [25]

$$\frac{d\boldsymbol{r}}{d\hat{t}} = \{\boldsymbol{r}, \hat{H}_{\rm real}\} = \frac{\partial\hat{H}_{\rm real}}{\partial\boldsymbol{p}}, \tag{11a}$$

$$\frac{d\boldsymbol{p}}{d\hat{t}} = \{\boldsymbol{p}, \hat{H}_{\rm real}\} + \hat{\mathcal{F}} = -\frac{\partial\hat{H}_{\rm real}}{\partial\boldsymbol{r}} + \hat{\mathcal{F}}, \tag{11b}$$

where $\hat{\mathcal{F}}$ denotes the nonconservative force that accounts for radiation-reaction effects. Following Ref. [13], we use [1]

$$\hat{\mathcal{F}} = \frac{1}{\nu\hat{\Omega}|\boldsymbol{r}\times\boldsymbol{p}|}\frac{dE}{dt}\boldsymbol{p}, \tag{12}$$

where $\hat{\Omega} \equiv M|\boldsymbol{r}\times\dot{\boldsymbol{r}}|/r^2$ is the dimensionless orbital frequency and dE/dt is the GW energy flux for quasicircular orbits obtained by summing over the modes (ℓ, m) as

$$\frac{dE}{dt} = \frac{\hat{\Omega}^2}{8\pi}\sum_{\ell=2}^{8}\sum_{m=0}^{\ell} m^2\left|\frac{\mathcal{R}}{M}h_{\ell m}\right|^2. \tag{13}$$

Here $\mathcal{R}$ is the distance to the source, and simply eliminates the dominant behavior of $h_{\ell m}$. We sum over positive m modes only since $|h_{\ell,m}| = |h_{\ell,-m}|$. Expressions for the modes $h_{\ell m}$ are given in the next section. In this paper, we restrict the calibration to nonprecessing binaries, and thus we omit the Hamilton equations of the spin variables.

It was demonstrated in previous work [37,58] that by replacing the radial component of the linear momentum $p_r \equiv (\boldsymbol{p}\cdot\boldsymbol{r})/r$ with p_{r^*}, which is the conjugate momentum of the EOB tortoise radial coordinate r^*, one can improve the numerical stability of the EOB equations of motion. This happens because p_r diverges when approaching $r^{\rm EOB}_+$ while p_{r^*} does not. In this paper we follow the definition of the EOB tortoise radial coordinate in Appendix A of Ref. [25].[2] However, when applying the tortoise coordinate transformation to the quartic term in Eq. (5), we get [25]

$$\mathcal{Q}_4(\boldsymbol{p}) \propto \frac{p^4_{r^*}}{r^2}\frac{D^2}{\Delta^4_t}(r^2 + \chi^2_{\rm Kerr})^4, \tag{14}$$

which clearly diverges at $r = r^{\rm EOB}_+$. As in the nonspinning case [27,37,58], we neglect contributions higher than 3PN order and rewrite Eq. (14) as

$$\mathcal{Q}_4(\boldsymbol{p}) \propto \frac{p^4_{r^*}}{r^2}(r^2 + \chi^2_{\rm Kerr})^4, \tag{15}$$

which is well behaved throughout the EOB orbital evolution.

Lastly, we integrate the EOB Hamilton equations. In order to get rid of any residual eccentricity when the

[1]The over-dot stands for d/dt.

[2]Note that all the formulas in Appendix A of Ref. [25] are written in physical dynamical variables, namely $\boldsymbol{R}$ and $\boldsymbol{P}$, while here we use reduced variables $\boldsymbol{r}$ and $\boldsymbol{p}$.

EOB orbital frequency is close to the initial frequency of the NR run, we start the EOB evolution at large separation, say $50M$, and use the quasispherical initial conditions developed in Ref. [13]. We stop the integration when the orbital frequency Ω reaches a maximum.

B. The effective-one-body waveforms

Following Refs. [24–27,37] we write the inspiral-plunge modes as

$$h_{\ell m}^{\rm insp\text{-}plunge} = h_{\ell m}^{\rm F} N_{\ell m}, \tag{16}$$

where the $h_{\ell m}^{\rm F}$ are the factorized modes developed in Refs. [37–39], and the $N_{\ell m}$ are non-quasicircular (NQC) corrections that model deviations from quasicircular motion, which is assumed when deriving the $h_{\ell m}^{\rm F}$. The factorized modes read

$$h_{\ell m}^{\rm F} = h_{\ell m}^{(N,\epsilon)} \hat{S}_{\rm eff}^{(\epsilon)} T_{\ell m} e^{i\delta_{\ell m}} (\rho_{\ell m})^{\ell}, \tag{17}$$

where ϵ is the parity of the waveform. All the factors entering the $h_{\ell m}^{\rm F}$ can be explicitly found in the Appendix. We emphasize here again that despite the fact that the GW energy flux in the comparable-mass case is known through 3PN order in the spin-orbit sector [44], the spin-orbit couplings in the factorized (or PN-expanded) modes have been computed only through 1.5PN order [39,45]. This limitation will degrade the performances of our spin EOB model for prograde orbits and large-spin values, as already observed in the test-particle limit in Refs. [28,39]. To improve the knowledge of spin effects in the GW modes, Refs. [25,39] added spin couplings in the test-particle limit through 4PN order in the factorized waveforms. However, since the mapping between the Kerr spin parameter in the test-particle limit and the black-hole spins in the comparable-mass case is not yet unambiguously determined [34,35], and since we do not have many NR spinning waveforms at our disposal to test the mapping, we decide not to include here the spinning test-particle-limit couplings in the factorized waveforms computed in Ref. [39]. We have checked before performing any calibration that EOB models with or without test-particle spin effects (with Kerr spin parameter $\chi_{\rm Kerr}$) give similar performances.

In all the calibrations of the nonspinning EOB model, two EOB adjustable parameters were needed to calibrate the EOB Hamilton equations—for example Refs. [26,27] used the 4PN and 5PN order coefficients in the EOB potential $A(r)$. As discussed in the previous section, for the EOB model adopted in this paper, the EOB nonspinning conservative dynamics depend so far only on the adjustable parameter K. We introduce a second EOB adjustable parameter in the nonconservative nonspinning EOB sector by adding a 4PN order nonspinning term in ρ_{22} and denote the coefficient of this unknown PN term by $\rho_{22}^{(4)}$ [see Eq. (A8a)]. This adjustable parameter enters the EOB Hamilton equations through the energy flux defined in Eq. (13).

As shown in Ref. [27], the NQC corrections of modes with $(\ell, m) \neq (2, 2)$ have marginal effects on the dynamics. Also, our goal in this work is to calibrate only the (2, 2) mode, so in the following we set $N_{\ell m} = 1$ for $(\ell, m) \neq (2, 2)$. We have[3]

$$N_{22} = \left[1 + \left(\frac{p_{r^*}}{r\hat{\Omega}}\right)^2 \left(a_1^{h_{22}} + \frac{a_2^{h_{22}}}{r} + \frac{a_3^{h_{22}}}{r^{3/2}} + \frac{a_4^{h_{22}}}{r^2} + \frac{a_5^{h_{22}}}{r^{5/2}}\right)\right] \times \exp\left[i \frac{p_{r^*}}{r\hat{\Omega}} \left(b_1^{h_{22}} + p_{r^*}^2 b_2^{h_{22}} + \frac{p_{r^*}^2}{r^{1/2}} b_3^{h_{22}} + \frac{p_{r^*}^2}{r} b_4^{h_{22}}\right)\right], \tag{18}$$

where $a_i^{h_{22}}$ (with $i = 1 \ldots 5$) are the (real) NQC amplitude coefficients and $b_i^{h_{22}}$ (with $i = 1 \ldots 4$) are the (real) NQC phase coefficients. We will explain in detail how these coefficients are determined at the end of this section.

The EOB merger-ringdown waveform is built as a linear superposition of the quasinormal modes (QNMs) of the final Kerr black hole [10,17,19,21,23,24,59], as

$$h_{22}^{\rm merger\text{-}RD}(t) = \sum_{n=0}^{N-1} A_{22n} e^{-i\sigma_{22n}(t - t_{\rm match}^{22})}, \tag{19}$$

where N is the number of overtones, A_{22n} is the complex amplitude of the n-th overtone, and $\sigma_{22n} = \omega_{22n} - i/\tau_{22n}$ is the complex frequency of this overtone with positive (real) frequency ω_{22n} and decay time τ_{22n}. The complex QNM frequencies are known functions of the mass and spin of the final Kerr black hole. Their numerical values can be found in Ref. [60]. The mass and spin of the final black hole, M_f and a_f, can be computed through analytical phenomenological formulas reproducing the NR predictions. Here, we adopt the formulas given in Eq. (8) of Ref. [61] and in Eqs. (1) and (3) of Ref. [62]. We notice that the formula for the final mass in Ref. [61] was obtained using numerical simulations of small-spin black-hole binaries with mildly unequal masses. As a consequence, the formula is not very accurate for the large-spin, unequal-mass binaries considered in this paper. However, other formulas available in the literature are either very accurate but only valid for equal-mass binaries [63], or have not been yet extensively tested against NR simulations [64,65]. Thus, for the time being we stick with Eq. (8) of Ref. [61], but we plan to construct a better formula in the future using all recent data in the literature.

Furthermore, we follow the hybrid matching procedure of Ref. [27] to fix the N complex amplitude coefficients A_{22n} in Eq. (19). We set up N complex linear equations by imposing that the inspiral-plunge and merger-ringdown

[3]Note that in Ref. [28] the $N_{\ell m}$ were written in terms of physical dynamical variables, rather than the reduced variables used here.

waveforms $h_{22}^{\text{inspiral-plunge}}$ and $h_{22}^{\text{merger-RD}}$ coincide on $N-2$ points (evenly sampled over a range $[t_{\text{match}}^{22}-\Delta t_{\text{match}}^{22}, t_{\text{match}}^{22}]$) and that their time derivatives $\dot{h}_{22}^{\text{inspiral-plunge}}$ and $\dot{h}_{22}^{\text{merger-RD}}$ coincide at $t_{\text{match}}^{22}-\Delta t_{\text{match}}^{22}$ and t_{match}^{22}. As in previous works, we introduce the EOB adjustable parameter $\Delta t_{\text{match}}^{22}$ which describes the size of the comb over which we impose continuous and smooth matching in order to determine the ringdown waveform.

In Refs. [24,27,28], pseudo QNMs (pQNMs) were proposed and applied to moderate the rise of the EOB GW frequency during the merger-ringdown transition—for example Sec. IIC of Ref. [27] discussed in some detail the advantage of using pQNMs for higher-order GW modes. In this paper, we find it useful to introduce a pQNM for the (2, 2) mode. Therefore, we choose $N=8$ in Eq. (19) and replace the highest overtone in the summation with this pQNM.

Finally, we build the full inspiral-plunge-merger-ringdown EOB waveform by joining the inspiral-plunge waveform $h_{22}^{\text{inspiral-plunge}}(t)$ and the merger-ringdown waveform $h_{22}^{\text{merger-RD}}(t)$ at the matching time t_{match}^{22} as

$$h_{22}^{\text{EOB}}(t) = h_{22}^{\text{inspiral-plunge}}(t)\theta(t_{\text{match}}^{22}-t) + h_{22}^{\text{merger-RD}}(t)\theta(t-t_{\text{match}}^{22}). \quad (20)$$

In Fig. 1, we summarize how the inspiral-plunge–merger-ringdown EOB waveform is constructed. Beyond the ISCO, the quasicircular inspiral waveform is followed by a short plunge waveform [4] where the radial motion is no longer negligible and NQC corrections quickly become important. The plunge ends roughly when the effective particle in the EOB description crosses the light-ring, which, in the nonspinning case, coincides approximately with the peak of EOB orbital frequency $\hat{\Omega}$ and waveform amplitude $|h_{22}|$. Until this moment, the GW radiation in the EOB description is obtained directly from the motion of the effective particle. After this moment that we identify as the merger, the direct emission of GWs from the effective particle is strongly attenuated and filtered by the potential barrier formed around the newborn black hole. Thus, in the EOB description the merger-ringdown waveform is no longer obtained from the motion of the effective particle, but it is built through a superposition of QNMs. This procedure of constructing the full EOB waveform, in particular, replacing the direct emission with a superposition of QNMs beyond the light ring, was first proposed in Refs. [10,13] for nonspinning and spinning comparable-mass black-hole binaries. It was inspired by the close-limit approximation [66] and results in Refs. [67,68] where it was observed that once the radially infalling particle is

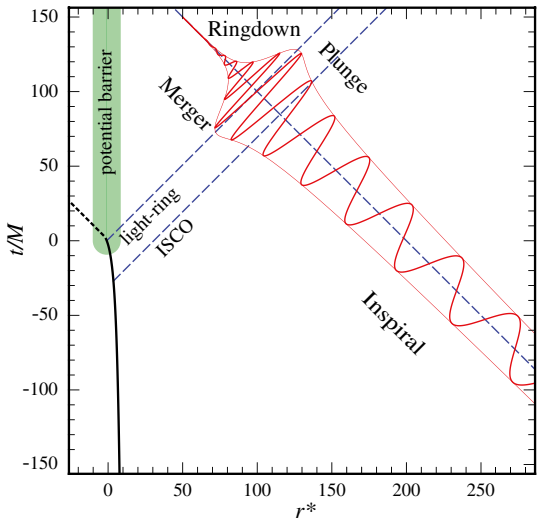

FIG. 1 (color online). We show in the spacetime diagram $(\hat{t}, r^*)$ the trajectory of the effective particle in the EOB description (black solid line in the left part of the diagram) and the EOB (2, 2) gravitational mode (red solid oscillating line) for an equal-mass nonspinning black-hole binary. Although we only need to evolve the EOB trajectory until the orbital frequency reaches its maximum (''light ring''), the model's dynamics allows the trajectory to continue to negative r^* (short-dashed black line in the left part of the diagram). The blue dashed lines represent $\hat{t}\pm r^*=$ const surfaces and ingoing/outgoing null rays. The EOB (2,2) mode is a function of the retarded time $\hat{t}-r^*$, plotted here orthogonal to $\hat{t}-r^*=$ const surfaces, at a finite $\hat{t}+r^*$ distance. The two outgoing null rays are drawn at the $\hat{t}-r^*$ retarded times when the EOB particle crosses the EOB ISCO and light-ring radii, respectively. The shaded green area is a rough sketch of the potential barrier around the newborn black hole.

inside the potential barrier which peaks around the light ring, the direct gravitational radiation from the particle is strongly filtered by the potential barrier. Part of the energy produced in the strong merger-burst remains stored in the resonant cavity of the geometry, i.e., inside the potential barrier, and what is released outside is just the ringdown signal. The nonlinear scattering of GW radiation (tails) against the curvature potential of the newborn black hole also contributes to the merger-ringdown waveform. Currently, in the EOB description the merger-ringdown waveform is effectively the tail of a δ-function impulse at merger. When spin effects are present, the overall picture depicted in Fig. 1 survives, but with some differences due to the fact that the EOB light-ring position, peak of the orbital-frequency $\hat{\Omega}$ and waveform amplitude $|h_{22}|$ can be displaced in time [28]. We notice that the physical picture of the merger-ringdown that emerged from the studies in Refs. [66–68] and was incorporated in the EOB description in Refs. [10,13], has also recently motivated the hybrid approach of Refs. [69,70].

We now continue our detailed review of how the EOB waveform is built and discuss how we fix the NQC coefficients in Eq. (18). Since we do not expect spin effects in

[4]The number of gravitational-wave cycles during the plunge scales roughly as $\nu^{-1/5}$ [10].

TABLE I. Exact NR-input values used in the right-hand side of Eqs. (21)–(25) to calibrate the EOB inspiral-plunge waveforms.

q	1	1/2	1/3	1/4	1/6	1	1
$\chi_1 = \chi_2$	0	0	0	0	0	+0.43655	−0.43757
$\lvert h^{\rm NR}_{22,\rm peak}\rvert$	0.3940	0.3446	0.2855	0.2403	0.1810	0.3942	0.3935
$10^4 M^2 \partial_t^2 \lvert h^{\rm NR}_{22,\rm peak}\rvert$	−10.3	−8.8	−6.9	−5.5	−3.9	−7.7	−12.4
$M\omega^{\rm NR}_{22,\rm peak}$	0.3593	0.3467	0.3324	0.3218	0.3084	0.3989	0.3342
$10^3 M^2 \dot{\omega}^{\rm NR}_{22,\rm peak}$	11.3	10.5	9.6	8.9	8.1	11.2	10.7

the NQC correction until 1.5PN order in either amplitude or phase, the coefficients $a_i^{h_{22}}$ with $i = 1, 2$ and $b_i^{h_{22}}$ with $i = 1, 2$ only depend on ν, while $a_i^{h_{22}}$ with $i = 4, 5$ and $b_i^{h_{22}}$ with $i = 3, 4$ are functions of ν linearly proportional to the spins $\chi_{1,2}$. The coefficient $a_3^{h_{22}}$ is given by the sum of a nonspinning term (dependent only on ν) and a spinning term (proportional to the spins $\chi_{1,2}$). In Sec. III we first calibrate the nonspinning waveforms, and then the spinning ones. Thus, we determine the ten coefficients in Eq. (18) in two steps. First, we set $\chi_1 = \chi_2 = 0$, thus $a_i^{h_{22}} = 0$ (with $i = 4, 5$) and $b_i^{h_{22}} = 0$ (with $i = 3, 4$) and calculate the values of the five NQC coefficients $a_i^{h_{22}}$ (with $i = 1, 2, 3$) and $b_i^{h_{22}}$ (with $i = 1, 2$) by imposing the following five conditions [27,28]:

(i) Let $t^{\Omega}_{\rm peak}$ be the time at which the EOB orbital frequency reaches its peak. Then, the peak of the EOB (2, 2) mode must happen at the matching time $t^{22}_{\rm match} = t^{\Omega}_{\rm peak} + \Delta t^{22}_{\rm peak}$, that is

$$\left.\frac{d|h^{\rm EOB}_{22}|}{dt}\right|_{t^{\Omega}_{\rm peak}+\Delta t^{22}_{\rm peak}} = 0, \tag{21}$$

where $\Delta t^{22}_{\rm peak}$ is an EOB adjustable parameter, which will be specified in Sec. III. We note that in Ref. [28] the quantity $\Delta t^{22}_{\rm peak}$ was computed by comparing the times at which the Teukolsky (2, 2) mode and the EOB orbital frequency reach their peaks. This was possible because the EOB trajectory was used in the Teukolsky equation to evolve the dynamics. However, in the NR simulation, we do not know what $\Delta t^{22}_{\rm peak}$ is, because the EOB dynamics does not determine the NR dynamics.

(ii) The amplitudes of the NR and EOB (2, 2) modes are the same,

$$|h^{\rm EOB}_{22}(t^{\Omega}_{\rm peak} + \Delta t^{22}_{\rm peak})| = |h^{\rm NR}_{22}(t^{\rm NR}_{\rm peak})|. \tag{22}$$

(iii) The curvatures of the amplitudes of the NR and EOB (2, 2) modes are the same,

$$\left.\frac{d^2|h^{\rm EOB}_{22}|}{dt^2}\right|_{t^{\Omega}_{\rm peak}+\Delta t^{22}_{\rm peak}} = \left.\frac{d^2|h^{\rm NR}_{22}|}{dt^2}\right|_{t^{\rm NR}_{\rm peak}}. \tag{23}$$

(iv) The GW frequencies of the NR and EOB (2, 2) modes are the same,

$$\omega^{\rm EOB}_{22}(t^{\Omega}_{\rm peak} + \Delta t^{22}_{\rm peak}) = \omega^{\rm NR}_{22}(t^{\rm NR}_{\rm peak}). \tag{24}$$

(v) The time derivatives of the GW frequency of the NR and EOB (2, 2) modes are the same,

$$\left.\frac{d\omega^{\rm EOB}_{22}}{dt}\right|_{t^{\Omega}_{\rm peak}+\Delta t^{22}_{\rm peak}} = \left.\frac{d\omega^{\rm NR}_{22}}{dt}\right|_{t^{\rm NR}_{\rm peak}}. \tag{25}$$

We summarize in Table I all the NR-input values that we use in the right-hand side of Eqs. (22)–(25). After the five nonspinning NQC coefficients have been computed, we plug them back into the EOB dynamics through the energy flux, start a new EOB evolution, generate a new EOB (2, 2) mode, and calculate new NQC coefficients. We repeat this procedure until the values of the NQC coefficients converge. Then, when calibrating spinning waveforms, we set $a_i^{h_{22}}$ and $b_i^{h_{22}}$ (with $i = 1, 2$), as well as the nonspinning part of $a_3^{h_{22}}$, to the values just calculated for $\chi_1 = \chi_2 = 0$, and apply the five conditions above in an iterative way, obtaining the final coefficients $a_i^{h_{22}}$ (with $i = 3, 4, 5$) and $b_i^{h_{22}}$ (with $i = 3, 4$). Note that in order to generate GW templates, this procedure can be computationally expensive, since to generate one EOB (2, 2) mode one has to evolve the dynamics a few times. The current computational cost of generating an EOB waveform long enough for the LIGO bandwidth varies between a fraction of a second to a few seconds,[5] depending on the masses. The iterative procedure can increase this cost by a factor of a few.

In order for the NQC coefficients to be effective in correcting the EOB mode peak, the latter has to occur in a region where the radial motion is comparable to or at least ∼30% of the tangential motion. Such a condition is in principle not a necessary requirement for the EOB model to work. In fact, the radial motion *is* expected to be strongly suppressed for almost extremal black holes, at least in the test-particle limit, since the ISCO coincides with the

[5]The time is measured by running a code that is not optimized in speed on a single CPU.

TABLE II. Summary of adjustable parameters of the spin EOB model considered in this paper. The values of the EOB adjustable parameters used in this paper are given in Eqs. (33)–(39). In addition, the NQC parameters $a_i^{h_{22}}$ and $b_i^{h_{22}}$ are fixed from NR-input values through Eqs. (21)–(25).

EOB dynamics adjustable parameters	EOB waveform adjustable parameters
K	$\rho_{22}^{(4)}$
$d_{\rm SO}$, $d_{\rm SS}$	$\Delta t^{22}_{\rm match}$, $\Delta t^{22}_{\rm peak}$
	$\omega_{22}^{\rm pQNM}$, $\tau_{22}^{\rm pQNM}$

horizon for $\chi = 1$ [71]. However, if the factorized (2, 2) mode, given by Eq. (17), differs substantially from the NR (2, 2) mode because of the lack of high-order spin-orbit terms, the inability of the NQC coefficient to change the waveform during the plunge at high spins may prevent the EOB model from working properly. This is because the NQC coefficients cannot artificially compensate the missing higher-order spin-orbit terms in the waveforms, as they partially do at low spins. In fact, we will see that this problem arises for $\chi_i \gtrsim 0.7$, making the EOB prototype waveforms unreliable for large positive spins.

We list in Table II all the EOB adjustable parameters that we exploit in this work to calibrate the EOB model to NR simulations.

III. EFFECTIVE-ONE-BODY CALIBRATION

In this section, we calibrate the EOB model using seven NR waveforms, namely, five nonspinning waveforms of mass ratios $q \equiv m_2/m_1 = 1, 1/2, 1/3, 1/4$ and $1/6$ and two equal-mass spinning waveforms with $\chi_1 = \chi_2 = +0.43655$ and $\chi_1 = \chi_2 = -0.43757$. The calibration is achieved by minimizing the amplitude and phase differences between the NR and EOB (2, 2) modes over the six EOB adjustable parameters: K, $d_{\rm SO}$ and $d_{\rm SS}$ in the EOB conservative dynamics, and $\rho_{22}^{(4)}$, $\Delta t^{22}_{\rm peak}$, $\Delta t^{22}_{\rm match}$, $\omega_{22}^{\rm pQNM}$ and $\tau_{22}^{\rm pQNM}$ in the EOB waveforms (see Table II).

A. Alignment of EOB and NR waveforms

When calibrating NR and EOB waveforms, we first align the waveforms at low frequency following the procedure of Refs. [24,25,27]. This procedure consists of minimizing the square of the difference between the NR and EOB (2, 2)-mode phases $\phi_{22}^{\rm NR}$ and $\phi_{22}^{\rm EOB}$, integrated over the time window (t_1, t_2),

$$\int_{t_1}^{t_2} [\phi_{22}^{\rm EOB}(t + t_0) + \phi_0 - \phi_{22}^{\rm NR}(t)]^2 dt, \tag{26}$$

with respect to the time shift t_0 and phase shift ϕ_0, where it is understood that $\phi_{22}^{\rm EOB}$ is computed for a chosen set of adjustable parameters. The time window (t_1, t_2) should: (i) begin as early as possible, where the NR and EOB GW-phase evolutions agree best, (ii) begin late enough to avoid the junk radiation present in the numerical simulation, (iii) be long enough to average over numerical noise, and (iv) extend from peak to peak (or trough to trough) over an integer number of oscillations in the GW frequency, which are caused by the residual eccentricity in the numerical initial conditions. In Table III, we list our choices of (t_1, t_2) for the seven numerical waveforms at our disposal. Each time window extends through 10 eccentricity oscillation cycles in the numerical frequency evolution.

Let $\bar{\phi}_0$ and $\bar{t}_0$ be the alignment parameters. Then, we define the phase and relative amplitude differences between the EOB and NR (2, 2) modes as follows:

$$\Delta\phi(t) = \phi_{22}^{\rm EOB}(t + \bar{t}_0) + \bar{\phi}_0 - \phi_{22}^{\rm NR}(t), \tag{27}$$

and

$$\left(\frac{\Delta A}{A}\right)(t) = \frac{|h_{22}^{\rm EOB}|(t + \bar{t}_0)}{|h_{22}^{\rm NR}|(t)} - 1. \tag{28}$$

We then define the global phase and relative amplitude differences over a time window (t_1, t_3) with

$$\Delta\phi_{\rm global} = \max_{t\in(t_1,t_3)} |\Delta\phi(t)|, \tag{29}$$

and

$$\left(\frac{\Delta A}{A}\right)_{\rm global} = \max_{t\in(t_1,t_3)} \left|\left(\frac{\Delta A}{A}\right)(t)\right|. \tag{30}$$

In the following, when measuring the difference between NR and EOB inspiral-plunge waveforms we set $t_3 = t^{22}_{\rm match}$, while when we measure the difference between full inspiral-merger-ringdown waveforms we use $t_3 = t_{\rm end}$, where $t_{\rm end}$ is chosen as late as possible into the ringdown stage, but before numerical errors due to gauge effects become noticeable [24]. We list the values of $t^{22}_{\rm match}$ and $t_{\rm end}$ for the seven NR waveforms in Table III.

B. Procedure to calibrate the EOB adjustable parameters

Recently, Ref. [28] computed the waveforms in the small-mass-ratio limit by evolving a time-domain Teukolsky equation in which the source term is evaluated using an EOB trajectory. It was found that there exists a time difference between the Teukolsky (2, 2)-mode amplitude peak and the EOB orbital-frequency peak. This difference is parametrized by the quantity $\Delta t^{22}_{\rm peak}$ introduced in Eq. (24). Table III in Ref. [28] lists this difference as a function of the Kerr spin parameter: for nonspinning and retrograde cases $-3M \lesssim \Delta t^{22}_{\rm peak} \lesssim 1.6M$, while for prograde cases $\Delta t^{22}_{\rm peak}$ decreases quickly as function of the spin. Let us consider $\chi_{\rm Kerr}$, which explicitly reads

$$\chi_{\rm Kerr} = (1 - 2\nu)\chi_{\rm S} + \sqrt{1 - 4\nu}\,\chi_{\rm A}, \tag{31}$$

and also define

TABLE III. We list the parameters t_1, t_2 entering the alignment procedure defined in Eq. (26), and the parameter t_3 (both $t^{22}_{\rm match}$ and $t_{\rm end}$) entering the computation of waveforms' differences in Eqs. (29) and (30).

q	1	1/2	1/3	1/4	1/6	1	1
$\chi_1 = \chi_2$	0	0	0	0	0	+0.43655	−0.43757
t_1/M	820	770	570	670	870	800	610
t_2/M	2250	2255	1985	1985	2310	2150	1850
$t^{22}_{\rm match}/M$	3943	3729	3515	3326	4892	3367	2402
$t_{\rm end}/M$	3990	3770	3560	3370	4940	3410	2430

$$\chi \equiv \chi_{\rm S} + \chi_{\rm A}\frac{\sqrt{1-4\nu}}{1-2\nu}, \tag{32}$$

where $\chi_{\rm S,A} \equiv (\chi_1 \pm \chi_2)/2$. For an equal-mass, equal-spin binary ($\nu = 1/4$, $\chi_1 = \chi$, $\chi_2 = \chi$) we have $\chi_{\rm Kerr} = \chi/2$, while in the test-particle limit we have $\chi_{\rm Kerr} = \chi$ (that is the spin parameter of the background spacetime). Therefore, inspired by the results in the test-particle limit, we assume here that for an equal-mass, equal-spin binary $\Delta t^{22}_{\rm peak}$ depends on the black-hole spins through χ. Explicitly we choose

$$\Delta t^{22}_{\rm peak} = \begin{cases} -2.5M & \text{if } \chi \le 0, \\ -2.5M - 1.77M\left(\frac{\chi}{0.437}\right)^4 & \text{if } \chi > 0, \end{cases} \tag{33}$$

which models qualitatively Table III in Ref. [28]. Following Refs. [24,25,27], we calibrate the EOB adjustable parameters in two steps. These steps are performed for each of our seven calibration NR waveforms separately, resulting in seven sets of calibration parameters. First, for each of the NR waveform at our disposal, we use $\Delta t^{22}_{\rm peak}$ in Eq. (33), insert the NR-input values from Table I into Eqs. (21)–(25), solve them iteratively for the NQC coefficients, and calibrate K, $\rho^{(4)}_{22}$ (or $d_{\rm SO}$ and $d_{\rm SS}$ if spins are present) by minimizing Eq. (29) with $t_3 = t^{22}_{\rm match}$. This process provides us with the EOB inspiral-plunge waveform. Second, to obtain the EOB merger-ringdown waveform, we calibrate the size of the comb $\Delta t^{22}_{\rm match}$ and the pQNM (complex) frequency by applying Eq. (29) with $t_3 = t_{\rm end}$. As in Ref. [27], we find that a constant value for the comb size, notably

$$\Delta t^{22}_{\rm match} = 7.5M, \tag{34}$$

gives a very good performance for all the different mass ratios and spins. A detailed study of the pQNM (complex) frequency has revealed that the best result is obtained when $\omega^{\rm pQNM}_{22}$ lies between the GW frequency $\omega^{\rm EOB}_{22}M/M_f$ at $t^{22}_{\rm match}$ and the frequency of the least-damped QNM ω_{220}, and when $\tau^{\rm pQNM}_{22}$ is (not much) shorter than τ_{220}. Specifically, we use the simple choice

$$\omega^{\rm pQNM}_{22} = \frac{1}{2}\left[\omega^{\rm EOB}_{22}(t^{22}_{\rm match})\frac{M}{M_f} + \omega_{220}\right], \tag{35a}$$

$$\tau^{\rm pQNM}_{22} = \frac{3}{10}\tau_{220}, \tag{35b}$$

for all different mass ratios and spins. Before ending this section, we discuss in more detail how we carry out the calibration of the parameters K, $\rho^{(4)}_{22}$, for the nonspinning sector, and the parameters $d_{\rm SO}$, $d_{\rm SS}$, for the spinning sector.

1. Calibrating nonspinning waveforms

In general, the adjustable parameters K and $\rho^{(4)}_{22}$ depend on the mass ratio and we assume that they are polynomial functions of ν. In principle, we should determine $K(\nu)$ and $\rho^{(4)}_{22}(\nu)$ by a global minimization of $\Delta\phi_{\rm global}$ and $(\Delta A/A)_{\rm global}$ [as defined in Eqs. (29) and (30) using $t_3 = t^{22}_{\rm match}$] with respect to the unknown coefficients entering the $K(\nu)$ and $\rho^{(4)}_{22}(\nu)$ polynomials. However, as in previous studies [26,27], we find a strong degeneracy among the EOB adjustable parameters, when calibrating each mass ratio separately. The degeneracy is partially broken when we combine all the available mass ratios together, but it is not completely lifted. In particular, different choices of $K(\nu)$ and $\rho^{(4)}_{22}(\nu)$ lead to EOB models that can match equally well with NR waveforms. We are thus relieved from a rigorous yet expensive global search and follow a simplified procedure to find satisfactory $K(\nu)$ and $\rho^{(4)}_{22}(\nu)$. First, we locate two points $(0.8154, -35)$ and $(1.188, -20)$ in the K-$\rho^{(4)}_{22}$ plane where $\Delta\phi_{\rm global} < 0.1$ rad and $(\Delta A/A)_{\rm global} < 0.1$ for $q = 1$ and $q = 1/6$ ($\nu = 0.25$ and $\nu = 0.1224$), respectively. We then determine a linear function $\rho^{(4)}_{22}(\nu)$ by imposing that $\rho^{(4)}_{22}(0.25) = -35$ and $\rho^{(4)}_{22}(0.1224) = -20$, leading to

$$\rho^{(4)}_{22}(\nu) = -5.6 - 117.6\nu. \tag{36}$$

At $q = 1/2$, $1/3$ and $1/4$, we choose $\rho^{(4)}_{22}$ according to Eq. (36) and determine the value of K that minimizes $\Delta\phi_{\rm global}$ and a range of K values that satisfy $\Delta\phi_{\rm global} < 0.1$ rad.

We now have a complete set of calibration parameters for each of our nonspinning NR waveforms. In order to obtain calibration parameters that interpolate between the

NR waveforms, we build a least-squares fit quadratic in ν against these K values. By construction, we fix two of the three free parameters in the fit by requiring that in the test-particle limit $K(\nu)$ reproduces the ISCO shift of Refs. [34,72,73] and that the optimal equal-mass value $K(0.25)$ is recovered exactly. Even with these two constraints and just one free parameter to fit, the residuals are within 1% (see Fig. 2). We find

$$K(\nu) = 1.447 - 1.715\nu - 3.246\nu^2. \tag{37}$$

Finally, since the iterative procedure to compute the NQC coefficients through Eqs. (21)–(25) can be expensive, we have parametrized them through quadratic fits, finding rather small residuals. Explicitly, we obtain

$$a_1^{h_{22}} = -12.68 + 75.42\nu - 106.6\nu^2, \tag{38a}$$
$$a_2^{h_{22}} = 101.5 - 757.3\nu + 1473\nu^2, \tag{38b}$$
$$a_3^{h_{22}} = -107.7 + 857.6\nu - 1776\nu^2, \tag{38c}$$
$$b_1^{h_{22}} = -1.464 + 12.82\nu - 60.10\nu^2, \tag{38d}$$
$$b_2^{h_{22}} = 7.477 - 85.26\nu + 353.3\nu^2. \tag{38e}$$

2. Calibrating spinning waveforms

When calibrating the EOB inspiral-plunge waveforms to the two NR equal-mass, equal-spin waveforms at our disposal ($\chi_1 = \chi_2 = +0.43655$ and $\chi_1 = \chi_2 = -0.43757$), we use the nonspinning EOB adjustable parameters K and $\rho_{22}^{(4)}$ in Eqs. (37) and (36), and calibrate the spinning EOB adjustable parameters $d_{\rm SO}$ and $d_{\rm SS}$. We reach this goal by building contour plots in the plane $d_{\rm SO}$-$d_{\rm SS}$ for $\Delta\phi_{\rm global}$ in Eq. (29) with $t_3 = t^{22}_{\rm match}$. We find that the contours of $\Delta\phi_{\rm global} = 0.2$ rads associated with the two NR spinning waveforms intersect each other for the following choice of the adjustable parameters

$$d_{\rm SO} = -69.5, \qquad d_{\rm SS} = 2.75. \tag{39}$$

Note that when computing the spinning NQC coefficients, we use the NQC coefficients parametrized in Eq. (38), and solve iteratively the five conditions (21)–(25) for $a_i^{h_{22}}$ ($i = 3, 4, 5$) and $b_i^{h_{22}}$ ($i = 3, 4$).[6]

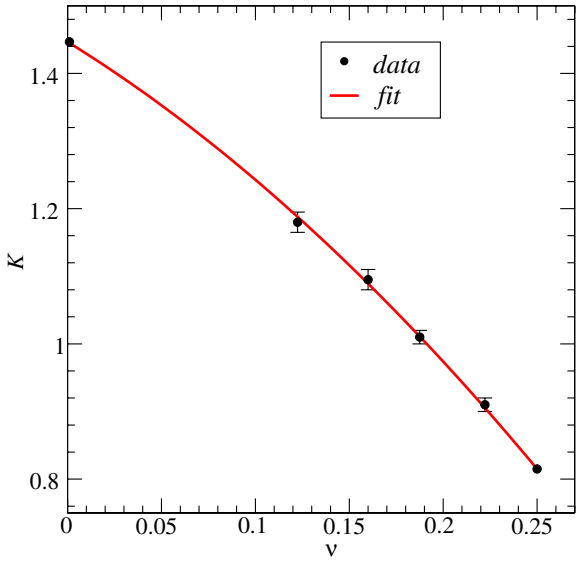

FIG. 2 (color online). We show the quadratic fit in ν for the adjustable parameter K. This parameter is calibrated using the five nonspinning NR waveforms, assuming $\rho_{22}^{(4)}(\nu)$ in Eq. (36). The error bars are determined by the intersection of the contours of $\Delta\phi_{\rm global} = 0.1$ rads with $\rho_{22}^{(4)}(\nu)$ for each mass ratio considered.

IV. A PROTOTYPE EFFECTIVE-ONE-BODY MODEL FOR NONPRECESSING SPINNING WAVEFORMS

We now build on the results of Sec. III, and also on recent outcomes of small-mass-ratio simulations produced by the Teukolsky equation [28], to construct a self-contained set of prescriptions to generate EOB inspiral-merger-ringdown waveforms in a larger region of the parameter space (ν, χ_1, χ_2) of the binary.

A. Interpolating the EOB model outside the domain of calibration

Since we only have seven NR waveforms at our disposal (and just two of them with spins), when extending the EOB model to regions of the parameter space without NR waveforms, we are forced to make assumptions on the behavior of the adjustable parameter $\Delta t^{22}_{\rm peak}$ and the NR-input values in Table I. In this work we assume that the 3-dimensional space (ν, χ_1, χ_2) can be treated as the 2-dimensional space (ν, χ). [Note that $\nu \in [0, 1/4]$ and $\chi \in [-1, 1]$.] More specifically, given a binary described by the parameters (ν, χ_1, χ_2) having in general $\chi_1 \neq \chi_2$, we consider an auxiliary equal-spin binary with parameters (ν, χ, χ), where χ is defined as in Eq. (32). With this choice, the auxiliary binary has the same value of $\chi_{\rm Kerr}$ as the original binary. We stress that the auxiliary binary is used only to extend the EOB adjustable parameters and the NR-input values to regions of the parameter space in which we do not have NR results. Of course the EOB dynamics and waveforms are computed for the original binary, not the auxiliary one.

Thus, in the prototype EOB model, the EOB adjustable parameter $\Delta t^{22}_{\rm peak}$ in Eq. (33) is evaluated using for χ the value from Eq. (32). To compute the spinning NQC coefficients in the prototype model, we need to prescribe the input values in the right-hand side of Eqs. (22)–(25) using

[6]Note that the NQC coefficient $a_3^{h_{22}}$ is solved for twice, first in the nonspinning calibration and then in the spinning one.

the parameters of the auxiliary binary. We proceed as follows. We only have knowledge of the NR-input values at merger for a few regions of the (ν, χ) parameter space. We can obtain the NR-input values along the curve $(\nu = 0, \chi)$ from the Teukolsky waveforms of Ref. [28]. In particular, both $|h^{\rm NR}_{22,\rm peak}|$ and $\partial_t^2|h^{\rm NR}_{22,\rm peak}|$ are set to 0 (since they are proportional to ν), while for $\omega^{\rm NR}_{22,\rm peak}$ and $\dot{\omega}^{\rm NR}_{22,\rm peak}$ we use the data in Table V of Ref. [28]. We can extract the peak information along the curve $(\nu = 1/4, \chi)$ from the three equal-mass waveforms used in the calibration of this paper, together with the two nearly extremal spin cases $\chi_1 = \chi_2 = -0.94905$ and $\chi_1 = \chi_2 = +0.9695$ (not used for the calibration of the adjustable parameters $d_{\rm SO}$ and $d_{\rm SS}$), which we will discuss in Sec. IV D. Along the curve $(\nu, \chi = 0)$ we can use the NR-input values of the nonspinning waveforms from Refs. [27,28]. In Table IV we list the fits for each NR-input value $f^{\rm NR} \in \{|h^{\rm NR}_{22,\rm peak}|, \partial_t^2|h^{\rm NR}_{22,\rm peak}|, \omega^{\rm NR}_{22,\rm peak}, \dot{\omega}^{\rm NR}_{22,\rm peak}\}$ in the test-particle and equal-mass limits. Along the nonspinning profile, fits quadratic in ν give a good description of the exact NR-input values, hence we assume that the dependence of $f^{\rm NR}$ on ν is quadratic as well and has the simple form

$$f^{\rm NR}(\nu, \chi) = c_2(\chi)\nu^2 + c_1(\chi)\nu + c_0(\chi). \tag{40}$$

We can fix two of the coefficients c_i by imposing that the test-particle limit and equal-mass cases are exactly recovered when $\nu = 0$ and $\nu = 1/4$, respectively. We can fit the third coefficient to the exact NR-input values along the nonspinning direction. This means that the fits along the nonspinning profile are not exactly recovered by the global fits $f^{\rm NR}(\nu, \chi)$, but we find that the residuals are negligible. Explicitly, we fit c_1 in the following expression

$$f^{\rm NR}(\nu, 0; c_1) = \{16[f^{\rm NR}(1/4, 0) - f^{\rm NR}(0, 0)] - 4c_1\}\nu^2 + c_1\nu + f^{\rm NR}(0, 0), \tag{41}$$

and denote the fitted value with $\bar{c}_1$. Finally, we extend the result outside the nonspinning profile assuming that the global fit reads

$$f^{\rm NR}(\nu, \chi) = \{16[f^{\rm NR}(1/4, \chi) - f^{\rm NR}(0, \chi)] - 4\bar{c}_1\}\nu^2 + \bar{c}_1\nu + f^{\rm NR}(0, \chi). \tag{42}$$

In Table V we list the values of $\bar{c}_1$ for the four NR-input values that are needed to compute the right-hand sides in Eqs. (22)–(25).

Having in hand $\Delta t^{22}_{\rm peak}$ and the NR-input values, we complete the construction of the prototype EOB model by fixing the EOB adjustable parameters K, $\rho^{(4)}_{22}$, and $d_{\rm SO}$, $d_{\rm SS}$ to the values in Eqs. (37), (36), and (39), respectively, employing the pQNM (complex) frequency in Eq. (35), the comb size in Eq. (34), and the NQC coefficients in Eqs. (38).

To test the robustness of the construction of the quantity $f^{\rm NR}(\nu, \chi)$, we study how the spinning NQC coefficients change across the plane (ν, χ). We focus on binaries with $\chi_1 = \chi_2 = \chi$. We compute iteratively the NQC amplitude coefficients $a_i^{h_{22}}$ (with $i = 3, 4, 5$) for different mass ratios in the range $1/100 \leq q \leq 1$ and for different spins in the range $-1 \leq \chi_i \lesssim 0.7$ $(i = 1, 2)$. Typically, we get convergence of the NQC coefficients within five iterations. Unfortunately, we cannot span larger, positive values of χ_i since the NQC corrections tend to diverge as the spin magnitude grows in the prograde case. The reason is that they become less effective in reshaping the EOB (2, 2) peak as prescribed by the fits $f^{\rm NR}(\nu, \chi)$. This happens because the peak of the EOB (2, 2) mode occurs too early in the evolution when the orbital motion is still quasicircular. Hence the NQC coefficients must be very large to compensate for the small values of $p_{r^*}/(r\hat{\Omega})$ and be able to reshape the EOB (2, 2) amplitude around the peak in a satisfactory way. As discussed earlier, this would not be a problem in principle if higher-order spin-orbit terms were known in the factorized waveforms, but, as a result of the lack of knowledge of those, our EOB prototype waveforms are reliable only up to $\chi_i \lesssim 0.7$.

B. Performance for nonspinning waveforms

In Figs. 3 and 4 we show how the inspiral-merger-ringdown EOB waveforms computed according to the prescriptions of Sec. IV A compare with the NR waveforms for two representative mass ratios $q = 1, 1/6$. In general, for all the nonspinning waveforms we find that the dephasing is typically within 0.1 rads up until $t^{22}_{\rm match}$ (merger time) and always within 0.2 rads when including the ringdown

TABLE IV. Fits of the NR-input values $f^{\rm NR}$ that are used to build the global fits in Eq. (42) for the test-particle and equal-mass limits.

$f^{\rm NR}$	Curve	Fit
$\lvert h^{\rm NR}_{22,\rm peak}\rvert$	$(\nu = 0, \chi)$	0
	$(\nu = 1/4, \chi)$	0.3961
$M^2\partial_t^2\lvert h^{\rm NR}_{22,\rm peak}\rvert$	$(\nu = 0, \chi)$	0
	$(\nu = 1/4, \chi)$	$10^{-3} \times (-1.007 + 0.5415\chi)$
$M\omega^{\rm NR}_{22,\rm peak}$	$(\nu = 0, \chi)$	$0.2758 - 0.08898\log(1 - \chi)$
	$(\nu = 1/4, \chi)$	$0.3604 + 0.08242\chi + 0.02794\chi^2$
$M^2\dot{\omega}^{\rm NR}_{22,\rm peak}$	$(\nu = 0, \chi)$	$10^{-3} \times [5.953 + (0.7199 + 1.210\chi)\log(1 - \chi)]$
	$(\nu = 1/4, \chi)$	0.01113

TABLE V. Fitted values of $\bar{c}_1$ for the four NR-input values as defined in Eq. (42).

	$\lvert h^{\rm NR}_{22,\rm peak}\rvert$	$M^2\partial_t^2\lvert h^{\rm NR}_{22,\rm peak}\rvert$	$M\omega^{\rm NR}_{22,\rm peak}$	$M^2\dot{\omega}^{\rm NR}_{22,\rm peak}$
$\bar{c}_1$	1.355	-2.5×10^{-3}	0.1935	0.01204

stage. The figures also show in dotted lines the NR phase and amplitude errors obtained by combining the extrapolation and resolution errors in quadrature. We notice that the EOB and NR amplitudes' agreement is remarkably good up to the merger time, while during the ringdown the relative amplitude difference may grow up to about 15%, approaching the estimated NR error.

In Ref. [27] the authors calibrated a different version of the nonspinning EOB model to the same set of nonspinning NR waveforms used in this paper, the main difference between the two EOB models being the choice of the EOB potential $A(r)$, as we discussed in Sec. II A. We find that the difference between the EOB inspiral-merger-ringdown waveforms and the NR waveforms in Ref. [27] is comparable to and for some mass ratios marginally worse than what we have achieved in this work using the prototype EOB model. The only noticeable qualitative difference is that the phase error of the prototype EOB model accumulates more slowly during the merger-ringdown transition because of the introduction of the pQNM in the (2, 2) mode. We point out that the inclusion of the pQNM (complex) frequency in the EOB merger-ringdown waveform is not strictly needed for the nonspinning case, but we use it even in this case for uniformity with the spinning sector, where the pQNM frequency is instead crucial.

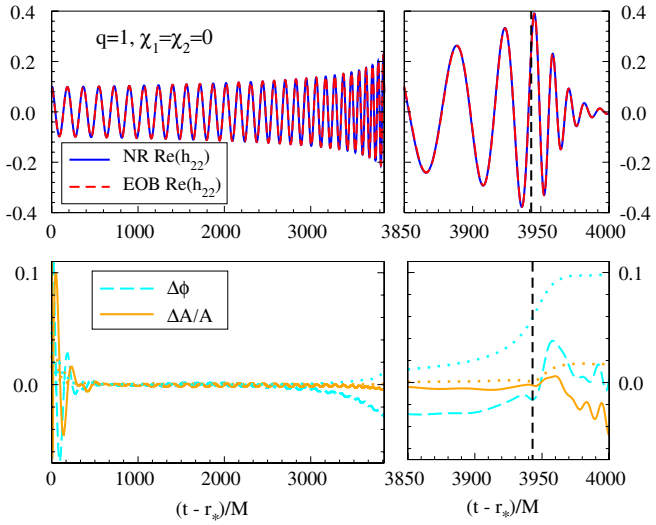

FIG. 3 (color online). Comparison of the NR and EOB (2, 2) mode for $q = 1$, $\chi_1 = \chi_2 = 0$. In the upper panels we show the comparison between the real part of the two waveforms, zooming into the merger region in the upper right plot. In the lower panels we show the dephasing and relative amplitude difference over the same time ranges as the upper panels. A vertical dashed line marks the position of the NR amplitude peak. The dotted curves are the NR errors.

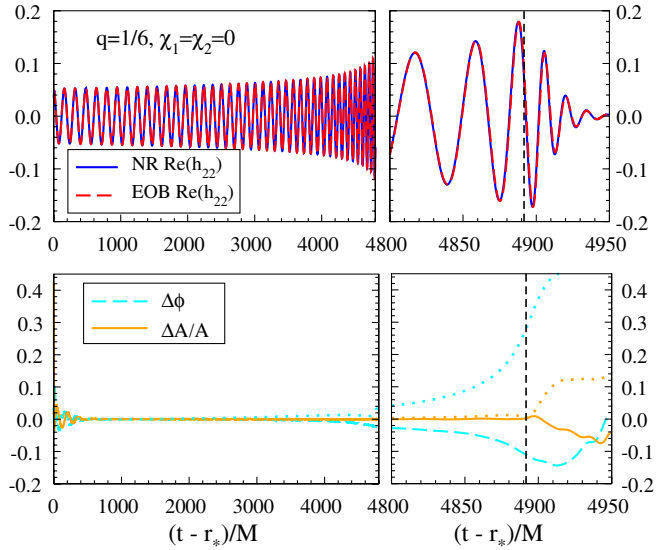

FIG. 4 (color online). Same as in Fig. 3 but for $q = 1/6$, $\chi_1 = \chi_2 = 0$.

We can quantify the differences between NR and EOB waveforms by computing the mismatch ($\mathcal{M}$), as defined in Eq. (43) of Ref. [27], which is one minus the overlap between two waveforms, weighted by the noise spectral density of the detector and maximized over the initial time, phase and binary parameters. If we use an Advanced LIGO noise curve, named ZERO_DET_HIGH_P in Ref. [4], we obtain that the $\mathcal{M}$, maximizing only over the initial phase and time, is always smaller than 0.001 when the binary total mass varies between $20M_\odot$ and $200M_\odot$. For these total masses, the NR waveforms start in band. We taper them using the Planck-taper window function [74] to reduce numerical artifacts. The width of the window function is set to the length of NR waveforms, ranging from $0.35(M/20M_\odot)$ to $0.65(M/20M_\odot)$ seconds. The window function smoothly rises from 0 to 1 in the first 0.0625 seconds and falls from 1 to 0 in the last 0.0125 seconds. We restrict the $\mathcal{M}$ integration to the frequency band for which NR waveform is available.

C. Performance for spinning waveforms

In Figs. 5 and 6 we present the results of the prototype EOB model for the two moderately spinning waveforms at our disposal. We observe that the choice (39) gives a larger dephasing for $\chi_1 = \chi_2 = +0.43655$ than for $\chi_1 = \chi_2 = -0.43757$ or the nonspinning runs. In fact at the merger time the dephasing for the $\chi_1 = \chi_2 = +0.43655$ waveform grows beyond the NR error. For the amplitude, we instead get a similar performance, on the same level as the other runs. The worse performance of the $\chi_1 = \chi_2 = +0.43655$ waveform can be explained by the more

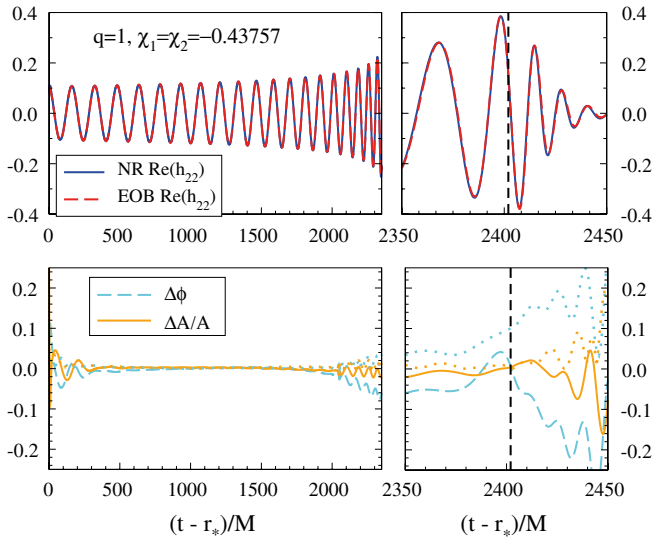

FIG. 5 (color online). Same as in Fig. 3 but for $q = 1$, $\chi_1 = \chi_2 = -0.43655$.

relativistic nature of this run. In fact, in this case the EOB ISCO moves to smaller radial separations as the spin parameter χ increases towards positive values (aligned runs). On the other hand, for negative values of χ (anti-aligned runs) the EOB ISCO moves outwards to a less relativistic regime and one expects a better behavior of the EOB model. This expectation is confirmed by the calibration of the $\chi_1 = \chi_2 = -0.43757$ run, for which we find that very good performances can be achieved in large regions of the EOB adjustable parameter space. Figure 5 shows that in this case the dephasing is well within the NR error at the merger time. For these spinning waveforms, we obtain that the $\mathcal{M}$, maximizing only over the initial phase and time, is always smaller than 0.003 when the binary total mass varies between $20M_\odot$ and $200M_\odot$.

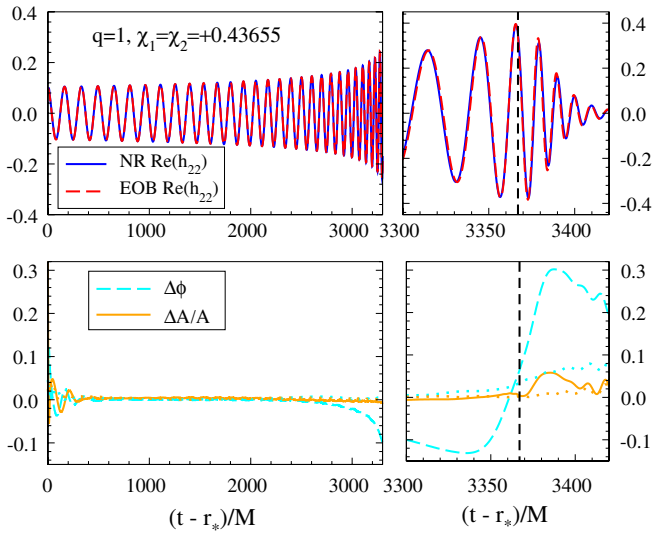

FIG. 6 (color online). Same as in Fig. 3 but for $q = 1$, $\chi_1 = \chi_2 = +0.43756$.

D. Performance for nearly extremal spin waveforms

Here we compare the EOB waveforms of the prototype model developed in Sec. IV A, against two equal-mass NR waveforms with nearly extremal spins: $\chi_1 = \chi_2 = -0.94905$ and $\chi_1 = \chi_2 = +0.9695$ [47,48]. We stress that these NR waveforms were not used when calibrating the spin EOB adjustable parameters $d_{\rm SO}$ and $d_{\rm SS}$ in Eq. (39). The only information that we used from these two nearly extremal spin waveforms was their NR-input values when building the fits $f^{\rm NR}(\nu, \chi)$.

As already discussed, when the spins are antialigned, the EOB ISCO moves towards larger radial separations, so that the binary is less relativistic throughout its orbital evolution as compared to the aligned configurations. Therefore, we expect that in this case the EOB model is more effective. The results in Fig. 7 for the case $\chi_1 = \chi_2 = -0.94905$ confirm this expectation. The dephasing grows up to about 2 rads during the ringdown, while the relative amplitude difference grows up to about 40%. Despite the large phase difference at merger, we find that, even without maximizing over the binary parameters but only the initial phase and time, the $\mathcal{M}$ is always smaller than 0.005 for systems with total mass between $20M_\odot$ and $200M_\odot$.

For the case $\chi_1 = \chi_2 = +0.9695$, which is outside the domain of validity of our prototype EOB model, we cannot successfully run the NQC iterations, since the NQC corrections are so large that they cause a divergent sequence of NQC coefficients. Nonetheless, we deem it interesting to

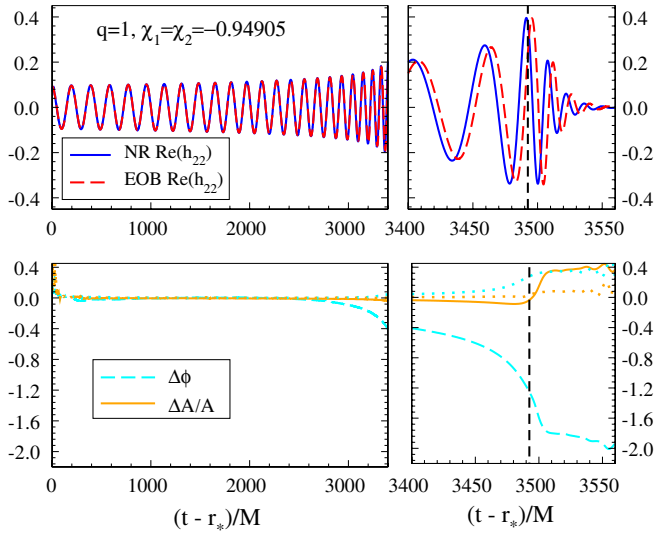

FIG. 7 (color online). Same as in Fig. 3 but for $q = 1$, $\chi_1 = \chi_2 = -0.94905$. This NR waveform was *not* used to calibrate the adjustable parameters $d_{\rm SO}$ and $d_{\rm SS}$. Alignment between the NR and EOB waveforms was performed using Eq. (26), with $t_1 = 860M$ and $t_2 = 2470M$.

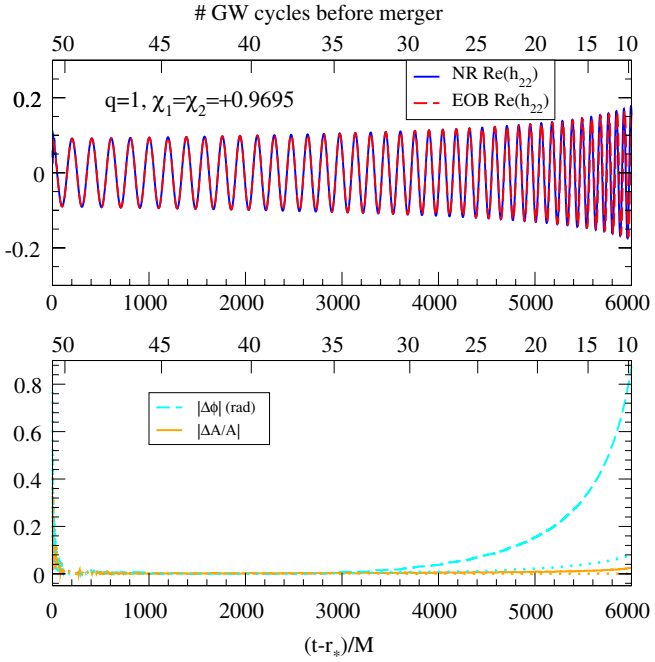

FIG. 8 (color online). Same as in Fig. 3 but for $q = 1$, $\chi_1 = \chi_2 = +0.9695$ and only the inspiral portion. This NR waveform was *not* used to calibrate the adjustable parameters $d_{\rm SO}$ and $d_{\rm SS}$. Also, in the aligned case our prototype EOB model only covers $\chi_{1,2} \lesssim 0.7$. Note that in this plot we do not include spinning NQC corrections in our EOB waveform. Alignment between the NR and EOB waveforms was performed using Eq. (26), with $t_1 = 1170M$ and $t_2 = 2790M$.

generate the EOB inspiral-plunge waveform where only the nonspinning NQC coefficients $a_i^{h_{22}}$ $(i = 1, 2, 3)$ and $b_i^{h_{22}}$ $(i = 1, 2)$ are used and compare it to the NR waveform. In Fig. 8 we show how our waveform performs. We notice that the NR waveform is very long, almost 50 GW cycles. The phase difference between the EOB and NR waveforms is smaller than 0.04 rads over the first 20 GW cycles, and then grows up to 0.18 rads during the subsequent 10 GW cycles and it becomes 0.9 rads when 10 GW cycles are left before merger. The fractional amplitude difference is only 3% when 10 GW cycles are left before merger.

It is worth emphasizing that although our prototype model is not yet able to generate merger-ringdown waveforms for spins larger than $+0.7$, nevertheless, as the comparison with the nearly extremal case $\chi_1 = \chi_2 = +0.9695$ has proven, the Hamiltonian of Refs. [34,35] and the resummed flux of Refs. [38,39] can evolve the EOB dynamics in this highly relativistic case beyond the orbital-frequency's peak, until $r \approx 1.9M$, without encountering unphysical features. This suggests that relevant strong-field effects are well grasped by the EOB dynamics and waveforms [34,35,38,39], at least as far as the NR runs used in this paper are concerned. Moreover, the large amplitude difference causing the NQC iteration to break down for large, positive spins was already observed in Refs. [28,39] where it was pointed out that it is important to improve the modeling of spin effects in the EOB waveform amplitude. Finally, as observed above, the breaking down of the NQC procedure in this highly relativistic case, although not a problem in principle if higher-order spin-orbit terms were known in the factorized waveforms, is due to the fact that the peak of the EOB (2, 2) mode occurs too early in the orbital evolution where non-quasicircular orbit effects are still negligible.

V. CONCLUSIONS

Using the EOB spin Hamiltonian in Refs. [34,35], the factorized waveforms in Refs. [38,39], and the adjustable parameters in Table II, we have developed a prototype EOB model for nonprecessing spinning black-hole binaries that can be used for detection purposes in LIGO and Virgo searches and employed for future calibrations [75]. The prototype model is built by first calibrating the EOB adjustable parameters against five nonspinning waveforms with mass ratios $q = 1, 1/2, 1/3, 1/4, 1/6$ and two equal-mass, equal-spin NR waveforms with moderate spins. Then, those results, at the interface with NR, are combined with recent results at the interface with black-hole perturbation theory [28]. The resulting prototype EOB model interpolates between calibrated points in the binary parameter space, and generates inspiral-merger-ringdown waveforms with any mass ratio and individual spin magnitudes $-1 \leq \chi_i \lesssim 0.7$. This EOB model has been implemented in the freely available LIGO Algorithm Library (LAL) [76] with the model name "SEOBNRv1".[7]

We found that the EOB waveforms generated with the prototype model agree with the NR waveforms used to calibrate them within $\sim$0.1 rads at merger for the nonspinning sector, and within $\sim$0.15 rads at merger for the spinning sector. In terms of amplitude differences at merger, both nonspinning and spinning runs agree to within 5%. The $\mathcal{M}$s for Advanced LIGO computed by maximizing only with respect to the initial phase and time are always smaller than 0.003 for binaries with total masses between $20M_\odot$ and $200M_\odot$.

We also compared the prototype EOB model to two equal-mass, equal-spin NR waveforms of black holes with nearly extremal spins, notably $\chi_i = -0.94905, +0.9695$. Those NR waveforms were not part of the original set of waveforms used to calibrate the EOB model. We found that for the antialigned case the prototype EOB model performs quite well for detection purposes, with $\mathcal{M}$s smaller than 0.003 without maximizing over the binary parameters, but only on initial phase and time. In the aligned case, which is highly relativistic due to a spin as

[7]Two nonspinning EOB models are also available in LAL, "EOBNRv1" and "EOBNRv2", which were calibrated to NR waveforms in Refs. [19,27].

large as $+0.9695$ (outside the range of validity of our prototype model), we compared the inspiral-plunge waveform for 40 GW cycles and found a dephasing of ~ 0.8 rad. During the last 10 GW cycles before merger the dephasing grows up to several radians. This nonsatisfactory performance during plunge and merger for large, positive spins is not surprising. In our prototype spin EOB model the factorized modes [39] used in the radiation-reaction force generate spin couplings in the GW energy flux at a PN order much lower than what is known today. In fact, the GW energy flux is currently known through 3PN order in the spin-orbit sector[8] [44] and 2PN order in the spin-spin sector. However, the -2 spin-weighted spherical harmonics that are used to build the factorized waveforms employed in this paper are known only through 1.5PN order in the spin-orbit sector [45]. Moreover, the performance we found for large-spin values and prograde orbits confirms what was already found in Ref. [28], where EOB waveforms in the test-particle limit could be calibrated to Teukolsky-type waveforms only up to a Kerr spin value of $\sim +0.7$. For larger spin values, the factorized waveforms start deviating from the exact ones even before reaching the ISCO [28,39].

The prototype spin EOB model can be improved in the future in different directions. First, the choice of the spin EOB adjustable parameters done in Sec. II was rather arbitrary and assumed that all gauge parameters that enter the spin EOB conservative dynamics are zero. Of course, it would have been difficult to carry out a more sophisticated study in this work considering that we had at our disposal only two equal-mass, equal-spin NR waveforms. When several more spin NR waveforms will be available, the spin EOB parameters (together with the nonspinning ones) should be explored and calibrated simultaneously against all the available NR waveforms. Second, it is urgent to compute higher-order PN spin-orbit terms in the -2 spin-weighted spherical harmonics and in the factorized modes, thus making the EOB spin model reliable also for large, positive spins, i.e., for $\chi_i > 0.7$. Third, the spin EOB Hamiltonian at 3.5PN order used in this paper predicts for large, positive spins that the position of the peak of the EOB orbital-frequency varies nonmonotonically as function of the spin and lies in a region which is not very relativistic. It would be important to correct this behavior calibrating the gauge parameters present in the spin EOB Hamiltonian. Fourth, recent results in Refs. [73,77–79] at the interface between PN theory and the self-force formalism, have allowed Ref. [80] to compute the nonspinning EOB potentials at all orders in PN theory, but linear in the symmetric mass ratio ν. These new results will be incorporated in the future to improve the nonspinning conservative dynamics of the prototype EOB model, and will be extended to include spin effects.

[8]Reference [48] found that the tail spin-orbit terms in the energy flux at 3PN order dominate all the other spin-orbit contributions and improve the agreement with NR waveforms.

ACKNOWLEDGMENTS

E. B., A. B., Y. P. and A. T. acknowledge support from NSF Grants No. PHY-0903631. A. B. also acknowledges support from NASA Grant No. NNX09AI81G. T. C., G. L., M. B., and M. S. are supported in part by grants from the Sherman Fairchild Foundation to Caltech and Cornell, and from the Brinson Foundation to Caltech; by NSF Grants No. PHY-0601459 and No. PHY-0652995 at Caltech; by NASA Grant No. NNX09AF97G at Caltech; by NSF Grants No. PHY-0652952 and No. PHY-0652929 at Cornell; and by NASA Grant No. NNX09AF96G at Cornell. H. P. gratefully acknowledges support from the NSERC of Canada, from Canada Research Chairs Program, and from the Canadian Institute for Advanced Research. E. B. acknowledges support from a CITA National Fellowship at the University of Guelph.

APPENDIX: EXPLICIT EXPRESSIONS OF THE FACTORIZED MODES

Using results from Refs. [24–27], we write here the explicit expressions of the factorized modes employed in Sec. II B. Even though we calibrated only the (2, 2) mode, we will provide expressions for all the modes up to $\ell = 8$, because they enter the computation of the energy flux in Eq. (13).

The terms $h^{(N,\epsilon)}_{\ell m}$ in Eq. (17) are the Newtonian modes. They read

$$h^{(N,\epsilon)}_{\ell m} = \frac{M\nu}{\mathcal{R}} n^{(\epsilon)}_{\ell m} c_{\ell+\epsilon}(\nu) V^{\ell}_{\Phi} Y^{\ell-\epsilon,-m}\left(\frac{\pi}{2}, \Phi\right), \tag{A1}$$

where $\mathcal{R}$ is the distance from the source; the $Y^{\ell m}(\Theta, \Phi)$ are the scalar spherical harmonics; we use $V^{\ell}_{\Phi} = v^{\ell+\epsilon}_{\Phi}$ with

$$v_{\Phi} = r_{\Omega}\hat{\Omega} = \hat{\Omega}\left(\frac{\partial \hat{H}_{\rm real}}{\partial p_{\Phi}}\bigg|_{p_r=0}\right)^{-2/3}, \tag{A2}$$

where $p_{\Phi} \equiv |\boldsymbol{r} \times \boldsymbol{p}|$. The functions $n^{(\epsilon)}_{\ell m}$ and $c_{\ell+\epsilon}(\nu)$ in Eq. (A1) read

$$n^{(0)}_{\ell m} = (im)^{\ell} \frac{8\pi}{(2\ell+1)!!}\sqrt{\frac{(\ell+1)(\ell+2)}{\ell(\ell-1)}}, \tag{A3a}$$

$$n^{(1)}_{\ell m} = -(im)^{\ell} \frac{16\pi i}{(2\ell+1)!!}\sqrt{\frac{(2\ell+1)(\ell+2)(\ell^2-m^2)}{(2\ell-1)(\ell+1)\ell(\ell-1)}}, \tag{A3b}$$

and

$$c_{\ell+\epsilon}(\nu) = \left(\frac{1}{2} - \frac{1}{2}\sqrt{1-4\nu}\right)^{\ell+\epsilon-1} + (-1)^{\ell+\epsilon}\left(\frac{1}{2} + \frac{1}{2}\sqrt{1-4\nu}\right)^{\ell+\epsilon-1}. \tag{A4}$$

The function $\hat{S}^{(\epsilon)}_{\rm eff}$ in Eq. (17) is an effective source term that in the circular-motion limit contains a pole at the

EOB light ring. It is given in terms of the EOB dynamics as

$$\hat{S}^{(\epsilon)}_{\rm eff}(r, p_{r_*}, p_\Phi, \mathbf{S}_1, \mathbf{S}_2) = \begin{cases} \hat{H}^{\rm eff}(r, p_{r_*}, p_\Phi, \mathbf{S}_1, \mathbf{S}_2), & \epsilon = 0, \\ \hat{L}_{\rm eff} = p_\Phi v_\Omega, & \epsilon = 1, \end{cases} \tag{A5}$$

where $v_\Omega = \hat{\Omega}^{1/3}$. The factor $T_{\ell m}$ in Eq. (17) resums the leading-order logarithms of tail effects, it reads

$$T_{\ell m} = \frac{\Gamma(\ell + 1 - 2imH_{\rm real}\Omega)}{\Gamma(\ell + 1)} \exp[\pi m \Omega H_{\rm real}] \times \exp[2im\Omega H_{\rm real} \log(2m\Omega r_0)], \tag{A6}$$

where $r_0 = 2M/\sqrt{e}$ [39].

In what follows we define

$$\delta m \equiv \frac{m_1 - m_2}{M}, \tag{A7a}$$

$$\chi_S \equiv \frac{\chi_1 + \chi_2}{2}, \tag{A7b}$$

$$\chi_A \equiv \frac{\chi_1 - \chi_2}{2}. \tag{A7c}$$

Also we use $\text{eulerlog}_m(v_\Omega^2) \equiv \gamma_E + \log 2 + \log m + 1/2 \log v_\Omega^2$, with γ_E being the Euler constant. We noticed that for even m the $\rho_{\ell m}$'s with spin contributions of Ref. [39] are ill-defined when $\delta m \to 0$. Thus, in this paper, for $m = 1, 3$ and $\ell \leq 4$, we replace the factor $(\rho_{\ell m})^\ell$ in Eq. (17) with the nonspinning (NS) limit of $(\rho_{\ell m})^\ell$ plus the spinning (S) part of the $f_{\ell m}$'s of Ref. [39]. More explicitly, the modes we used read [38,39]

$$\rho_{22} = 1 + \left(\frac{55\nu}{84} - \frac{43}{42}\right)v_\Omega^2 - \frac{2}{3}[\chi_S(1-\nu) + \chi_A \delta m]v_\Omega^3 + \left(\frac{19583\nu^2}{42336} - \frac{33025\nu}{21168} - \frac{20555}{10584}\right)v_\Omega^4 + \left(\frac{10620745\nu^3}{39118464} - \frac{6292061\nu^2}{3259872} + \frac{41\pi^2\nu}{192} - \frac{48993925\nu}{9779616} - \frac{428\,\text{eulerlog}_2(v_\Omega^2)}{105} + \frac{1556919113}{122245200}\right)v_\Omega^6 + \left(\nu\rho_{22}^{(4)} + \frac{9202\,\text{eulerlog}_2(v_\Omega^2)}{2205} - \frac{387216563023}{160190110080}\right)v_\Omega^8 + \left(\frac{439877\,\text{eulerlog}_2(v_\Omega^2)}{55566} - \frac{16094530514677}{533967033600}\right)v_\Omega^{10}, \tag{A8a}$$

$$\rho_{21}^{L\,\rm NS} = 1 + \left(\frac{23\nu}{84} - \frac{59}{56}\right)v_\Omega^2 + \left(\frac{617\nu^2}{4704} - \frac{10993\nu}{14112} - \frac{47009}{56448}\right)v_\Omega^4 + \left(\frac{7613184941}{2607897600} - \frac{107\,\text{eulerlog}_1(v_\Omega^2)}{105}\right)v_\Omega^6 + \left(\frac{6313\,\text{eulerlog}_1(v_\Omega^2)}{5880} - \frac{1168617463883}{911303737344}\right)v_\Omega^8 + \left(\frac{5029963\,\text{eulerlog}_1(v_\Omega^2)}{5927040} - \frac{63735873771463}{16569158860800}\right)v_\Omega^{10}, \tag{A8b}$$

where $\rho_{22}^{(4)}$ is a nonspinning EOB adjustable parameter, which is determined through the calibration of the nonspinning NR waveforms,

$$\rho_{33}^{\rm NS} = 1 + \left(\frac{2\nu}{3} - \frac{7}{6}\right)v_\Omega^2 + \left(\frac{149\nu^2}{330} - \frac{1861\nu}{990} - \frac{6719}{3960}\right)v_\Omega^4 + \left(\frac{3203101567}{227026800} - \frac{26\,\text{eulerlog}_3(v_\Omega^2)}{7}\right)v_\Omega^6 + \left(\frac{13\,\text{eulerlog}_3(v_\Omega^2)}{3} - \frac{57566572157}{8562153600}\right)v_\Omega^8, \tag{A9a}$$

$$\rho_{32}^{L} = 1 - \frac{4\nu}{3(3\nu-1)}\chi_S v_\Omega + \frac{320\nu^2 - 1115\nu + 328}{270(3\nu-1)}v_\Omega^2 + \frac{3085640\nu^4 - 20338960\nu^3 - 4725605\nu^2 + 8050045\nu - 1444528}{1603800(1-3\nu)^2}v_\Omega^4 + \left(\frac{5849948554}{940355325} - \frac{104\,\text{eulerlog}_2(v_\Omega^2)}{63}\right)v_\Omega^6 + \left(\frac{17056\,\text{eulerlog}_2(v_\Omega^2)}{8505} - \frac{10607269449358}{3072140846775}\right)v_\Omega^8, \tag{A9b}$$

$$\rho_{31}^{\rm NS} = 1 - \left(\frac{2\nu}{9} + \frac{13}{18}\right)v_\Omega^2 + \left(-\frac{829\nu^2}{1782} - \frac{1685\nu}{1782} + \frac{101}{7128}\right)v_\Omega^4 + \left(\frac{11706720301}{6129723600} - \frac{26\,\text{eulerlog}_1(v_\Omega^2)}{63}\right)v_\Omega^6 + \left(\frac{169\,\text{eulerlog}_1(v_\Omega^2)}{567} + \frac{2606097992581}{4854741091200}\right)v_\Omega^8, \tag{A9c}$$

$$\rho_{44} = 1 + \frac{2625\nu^2 - 5870\nu + 1614}{1320(3\nu - 1)} v_\Omega^2 - \frac{1}{15(1-3\nu)}[(42\nu^2 - 41\nu + 10)\chi_S + (10 - 39\nu)\delta m \chi_A] v_\Omega^3 + \frac{1252563795\nu^4 - 6733146000\nu^3 - 313857376\nu^2 + 2338945704\nu - 511573572}{317116800(1-3\nu)^2} v_\Omega^4 + \left(\frac{16600939332793}{1098809712000} - \frac{12568\,\mathrm{eulerlog}_4(v_\Omega^2)}{3465}\right) v_\Omega^6, \tag{A10a}$$

$$\rho_{43}^{L\,\mathrm{NS}} = 1 + \frac{160\nu^2 - 547\nu + 222}{176(2\nu - 1)} v_\Omega^2 - \frac{6894273}{7047040} v_\Omega^4 + \left(\frac{1664224207351}{195343948800} - \frac{1571\mathrm{eulerlog}_3(v_\Omega^2)}{770}\right) v_\Omega^6, \tag{A10b}$$

$$\rho_{42} = 1 + \frac{285\nu^2 - 3530\nu + 1146}{1320(3\nu - 1)} v_\Omega^2 - \frac{1}{15(1-3\nu)}[(78\nu^2 - 59\nu + 10)\chi_S + (10 - 21\nu)\delta m \chi_A] v_\Omega^3 + \frac{-379526805\nu^4 - 3047981160\nu^3 + 1204388696\nu^2 + 295834536\nu - 114859044}{317116800(1-3\nu)^2} v_\Omega^4 + \left(\frac{848238724511}{219761942400} - \frac{3142\,\mathrm{eulerlog}_2(v_\Omega^2)}{3465}\right) v_\Omega^6, \tag{A10c}$$

$$\rho_{41}^{L\,\mathrm{NS}} = 1 + \frac{288\nu^2 - 1385\nu + 602}{528(2\nu - 1)} v_\Omega^2 - \frac{7775491}{21141120} v_\Omega^4 + \left(\frac{1227423222031}{1758095539200} - \frac{1571\,\mathrm{eulerlog}_1(v_\Omega^2)}{6930}\right) v_\Omega^6, \tag{A10d}$$

$$\rho_{55} = 1 - \frac{512\nu^2 - 1298\nu + 487}{390(2\nu - 1)} v_\Omega^2 - \frac{3353747}{2129400} v_\Omega^4, \tag{A11a}$$

$$\rho_{54}^L = 1 + \frac{33320\nu^3 - 127610\nu^2 + 96019\nu - 17448}{13650(5\nu^2 - 5\nu + 1)} v_\Omega^2 - \frac{16213384}{15526875} v_\Omega^4, \tag{A11b}$$

$$\rho_{53} = 1 + \frac{176\nu^2 - 850\nu + 375}{390(2\nu - 1)} v_\Omega^2 - \frac{410833}{709800} v_\Omega^4, \tag{A11c}$$

$$\rho_{52}^L = 1 + \frac{21980\nu^3 - 104930\nu^2 + 84679\nu - 15828}{13650(5\nu^2 - 5\nu + 1)} v_\Omega^2 - \frac{7187914}{15526875} v_\Omega^4, \tag{A11d}$$

$$\rho_{51} = 1 + \frac{8\nu^2 - 626\nu + 319}{390(2\nu - 1)} v_\Omega^2 - \frac{31877}{304200} v_\Omega^4, \tag{A11e}$$

$$\rho_{66} = 1 + \frac{273\nu^3 - 861\nu^2 + 602\nu - 106}{84(5\nu^2 - 5\nu + 1)} v_\Omega^2 - \frac{1025435}{659736} v_\Omega^4, \tag{A12a}$$

$$\rho_{65}^L = 1 + \frac{220\nu^3 - 910\nu^2 + 838\nu - 185}{144(3\nu^2 - 4\nu + 1)} v_\Omega^2, \tag{A12b}$$

$$\rho_{64} = 1 + \frac{133\nu^3 - 581\nu^2 + 462\nu - 86}{84(5\nu^2 - 5\nu + 1)} v_\Omega^2 - \frac{476887}{659736} v_\Omega^4, \tag{A12c}$$

$$\rho_{63}^L = 1 + \frac{156\nu^3 - 750\nu^2 + 742\nu - 169}{144(3\nu^2 - 4\nu + 1)} v_\Omega^2, \tag{A12d}$$

$$\rho_{62} = 1 + \frac{49\nu^3 - 413\nu^2 + 378\nu - 74}{84(5\nu^2 - 5\nu + 1)} v_\Omega^2 - \frac{817991}{3298680} v_\Omega^4, \tag{A12e}$$

$$\rho_{61}^L = 1 + \frac{124\nu^3 - 670\nu^2 + 694\nu - 161}{144(3\nu^2 - 4\nu + 1)} v_\Omega^2, \tag{A12f}$$

$$\rho_{77} = 1 + \frac{1380\nu^3 - 4963\nu^2 + 4246\nu - 906}{714(3\nu^2 - 4\nu + 1)} v_\Omega^2, \tag{A13a}$$

$$\rho_{76}^L = 1 + \frac{6104\nu^4 - 29351\nu^3 + 37828\nu^2 - 16185\nu + 2144}{1666(7\nu^3 - 14\nu^2 + 7\nu - 1)} v_\Omega^2, \tag{A13b}$$

$$\rho_{75} = 1 + \frac{804\nu^3 - 3523\nu^2 + 3382\nu - 762}{714(3\nu^2 - 4\nu + 1)} v_\Omega^2, \tag{A13c}$$

$$\rho_{74}^L = 1 + \frac{41076\nu^4 - 217959\nu^3 + 298872\nu^2 - 131805\nu + 17756}{14994(7\nu^3 - 14\nu^2 + 7\nu - 1)} v_\Omega^2, \tag{A13d}$$

$$\rho_{73} = 1 + \frac{420\nu^3 - 2563\nu^2 + 2806\nu - 666}{714(3\nu^2 - 4\nu + 1)} v_\Omega^2, \tag{A13e}$$

$$\rho_{72}^L = 1 + \frac{32760\nu^4 - 190239\nu^3 + 273924\nu^2 - 123489\nu + 16832}{14994(7\nu^3 - 14\nu^2 + 7\nu - 1)} v_\Omega^2, \tag{A13f}$$

$$\rho_{71} = 1 + \frac{228\nu^3 - 2083\nu^2 + 2518\nu - 618}{714(3\nu^2 - 4\nu + 1)} v_\Omega^2, \tag{A13g}$$

$$\rho_{88} = 1 + \frac{3482 - 26778\nu + 64659\nu^2 - 53445\nu^3 + 12243\nu^4}{2736(-1 + 7\nu - 14\nu^2 + 7\nu^3)} v_\Omega^2, \tag{A14a}$$

$$\rho_{87}^L = 1 + \frac{23478 - 154099\nu + 309498\nu^2 - 207550\nu^3 + 38920\nu^4}{18240(-1 + 6\nu - 10\nu^2 + 4\nu^3)} v_\Omega^2, \tag{A14b}$$

$$\rho_{86} = 1 + \frac{1002 - 7498\nu + 17269\nu^2 - 13055\nu^3 + 2653\nu^4}{912(-1 + 7\nu - 14\nu^2 + 7\nu^3)} v_\Omega^2, \tag{A14c}$$

$$\rho_{85}^L = 1 + \frac{4350 - 28055\nu + 54642\nu^2 - 34598\nu^3 + 6056\nu^4}{3648(-1 + 6\nu - 10\nu^2 + 4\nu^3)} v_\Omega^2, \tag{A14d}$$

$$\rho_{84} = 1 + \frac{2666 - 19434\nu + 42627\nu^2 - 28965\nu^3 + 4899\nu^4}{2736(-1 + 7\nu - 14\nu^2 + 7\nu^3)} v_\Omega^2, \tag{A14e}$$

$$\rho_{83}^L = 1 + \frac{20598 - 131059\nu + 249018\nu^2 - 149950\nu^3 + 24520\nu^4}{18240(-1 + 6\nu - 10\nu^2 + 4\nu^3)} v_\Omega^2, \tag{A14f}$$

$$\rho_{82} = 1 + \frac{2462 - 17598\nu + 37119\nu^2 - 22845\nu^3 + 3063\nu^4}{2736(-1 + 7\nu - 14\nu^2 + 7\nu^3)} v_\Omega^2, \tag{A14g}$$

$$\rho_{81}^L = 1 + \frac{20022 - 126451\nu + 236922\nu^2 - 138430\nu^3 + 21640\nu^4}{18240(-1 + 6\nu - 10\nu^2 + 4\nu^3)} v_\Omega^2, \tag{A14h}$$

and

$$f_{21}^{L\,\mathrm{S}} = -\frac{3}{2}\left(\chi_S + \frac{\chi_A}{\delta m}\right) v_\Omega, \tag{A15a}$$

$$f_{33}^{\mathrm{S}} = -\left[\chi_S\left(2 - \frac{5}{2}\nu\right) + \frac{\chi_A}{\delta m}\left(2 - \frac{19}{2}\nu\right)\right] v_\Omega^3, \tag{A15b}$$

$$f_{31}^{\mathrm{S}} = -\left[\chi_S\left(2 - \frac{11}{2}\nu\right) + \frac{\chi_A}{\delta m}\left(2 - \frac{13}{2}\nu\right)\right] v_\Omega^3, \tag{A15c}$$

$$f_{43}^{L\,\mathrm{S}} = f_{41}^{L\,\mathrm{S}} = -\frac{5\nu}{2(2\nu - 1)}\left(\chi_S - \frac{\chi_A}{\delta m}\right) v_\Omega. \tag{A15d}$$

Finally, we give the explicit expression of the phase term

$$\delta_{22} = \frac{7}{3}(\hat{\Omega} H_{\mathrm{real}}) + \frac{428\pi}{105}(\hat{\Omega} H_{\mathrm{real}})^2 + \left(\frac{1712\pi^2}{315} - \frac{2203}{81}\right)(\hat{\Omega} H_{\mathrm{real}})^3 - 24\nu v_\Omega^5. \tag{A15}$$

[1] B. Abbott *et al.* (LIGO Scientific Collaboration), Rep. Prog. Phys. **72**, 076901 (2009).
[2] H. Grote (LIGO Scientific Collaboration), Classical Quantum Gravity **25**, 114043 (2008).
[3] F. Acernese, M. Alshourbagy, P. Amico, F. Antonucci, S. Aoudia *et al.*, Classical Quantum Gravity **25**, 184001 (2008).
[4] D. Shoemaker (LIGO Collaboration), LIGO Document Report No. T0900288-v3, https://dcc.ligo.org/cgi-bin/DocDB/ShowDocument?docid=2974 (2010).
[5] M. Sasaki and H. Tagoshi, Living Rev. Relativity **6**, 6 (2003).
[6] L. Blanchet, Living Rev. Relativity **9**, 4 (2006).
[7] T. Futamase and Y. Itoh, Living Rev. Relativity **10**, 2 (2007).
[8] W. D. Goldberger and I. Z. Rothstein, Phys. Rev. D **73**, 104029 (2006).
[9] A. Buonanno and T. Damour, Phys. Rev. D **59**, 084006 (1999).
[10] A. Buonanno and T. Damour, Phys. Rev. D **62**, 064015 (2000).
[11] T. Damour, P. Jaranowski, and G. Schafer, Phys. Rev. D **62**, 084011 (2000).
[12] T. Damour, Phys. Rev. D **64**, 124013 (2001).
[13] A. Buonanno, Y. Chen, and T. Damour, Phys. Rev. D **74**, 104005 (2006).
[14] F. Pretorius, Phys. Rev. Lett. **95**, 121101 (2005).
[15] J. G. Baker, J. Centrella, D.-I. Choi, M. Koppitz, and J. van Meter, Phys. Rev. Lett. **96**, 111102 (2006).
[16] M. Campanelli, C. O. Lousto, P. Marronetti, and Y. Zlochower, Phys. Rev. Lett. **96**, 111101 (2006).
[17] A. Buonanno, G. B. Cook, and F. Pretorius, Phys. Rev. D **75**, 124018 (2007).
[18] Y. Pan, A. Buonanno, J. G. Baker, J. Centrella, B. J. Kelly *et al.*, Phys. Rev. D **77**, 024014 (2008).
[19] A. Buonanno, Y. Pan, J. G. Baker, J. Centrella, B. J. Kelly *et al.*, Phys. Rev. D **76**, 104049 (2007).
[20] T. Damour and A. Nagar, Phys. Rev. D **77**, 024043 (2008).
[21] T. Damour, A. Nagar, E. N. Dorband, D. Pollney, and L. Rezzolla, Phys. Rev. D **77**, 084017 (2008).
[22] M. Boyle, A. Buonanno, L. E. Kidder, A. H. Mroue, Y. Pan *et al.*, Phys. Rev. D **78**, 104020 (2008).
[23] T. Damour, A. Nagar, M. Hannam, S. Husa, and B. Brugmann, Phys. Rev. D **78**, 044039 (2008).
[24] A. Buonanno, Y. Pan, H. P. Pfeiffer, M. A. Scheel, L. T. Buchman *et al.*, Phys. Rev. D **79**, 124028 (2009).
[25] Y. Pan, A. Buonanno, L. T. Buchman, T. Chu, L. E. Kidder *et al.*, Phys. Rev. D **81**, 084041 (2010).
[26] T. Damour and A. Nagar, Phys. Rev. D **79**, 081503 (2009).
[27] Y. Pan, A. Buonanno, M. Boyle, L. T. Buchman, L. E. Kidder *et al.*, Phys. Rev. D **84**, 124052 (2011).
[28] E. Barausse, A. Buonanno, S. A. Hughes, G. Khanna, S. O'Sullivan *et al.*, Phys. Rev. D **85**, 024046 (2012).
[29] J. Abadie *et al.* (The LIGO Scientific Collaboration and the Virgo Collaboration), Phys. Rev. D **83**, 122005 (2011).
[30] J. Abadie *et al.* (The LIGO Scientific Collaboration and the Virgo Collaboration), arXiv:1201.5999.
[31] P. Ajith, S. Babak, Y. Chen, M. Hewitson, B. Krishnan *et al.*, Phys. Rev. D **77**, 104017 (2008).
[32] T. Damour, P. Jaranowski, and G. Schafer, Phys. Rev. D **78**, 024009 (2008).
[33] E. Barausse, E. Racine, and A. Buonanno, Phys. Rev. D **80**, 104025 (2009).
[34] E. Barausse and A. Buonanno, Phys. Rev. D **81**, 084024 (2010).
[35] E. Barausse and A. Buonanno, Phys. Rev. D **84**, 104027 (2011).
[36] A. Nagar, Phys. Rev. D **84**, 084028 (2011).
[37] T. Damour and A. Nagar, Phys. Rev. D **76**, 064028 (2007).
[38] T. Damour, B. R. Iyer, and A. Nagar, Phys. Rev. D **79**, 064004 (2009).
[39] Y. Pan, A. Buonanno, R. Fujita, E. Racine, and H. Tagoshi, Phys. Rev. D **83**, 064003 (2011).
[40] R. Fujita and B. R. Iyer, Phys. Rev. D **82**, 044051 (2010).
[41] R. Fujita, arXiv:1104.5615.
[42] L. E. Kidder, Phys. Rev. D **77**, 044016 (2008).
[43] L. Blanchet, G. Faye, B. R. Iyer, and S. Sinha, Classical Quantum Gravity **25**, 165003 (2008).
[44] L. Blanchet, A. Buonanno, and G. Faye, Phys. Rev. D **84**, 064041 (2011).
[45] K. G. Arun, A. Buonanno, G. Faye, and E. Ochsner, Phys. Rev. D **79**, 104023 (2009).
[46] T. Chu, H. P. Pfeiffer, and M. A. Scheel, Phys. Rev. D **80**, 124051 (2009).
[47] G. Lovelace, M. A. Scheel, and B. Szilagyi, Phys. Rev. D **83**, 024010 (2011).
[48] G. Lovelace, M. Boyle, M. A. Scheel, and B. Szilágyi, Classical Quantum Gravity **29**, 045003 (2012).
[49] T. Damour, P. Jaranowski, and G. Schafer, Phys. Rev. D **62**, 021501 (2000); **63**, 029903(E) (2000).
[50] R. A. Porto and I. Z. Rothstein, Phys. Rev. Lett. **97**, 021101 (2006).
[51] R. A. Porto, Phys. Rev. D **73**, 104031 (2006).
[52] R. A. Porto and I. Z. Rothstein, Phys. Rev. D **78**, 044013 (2008).
[53] R. A. Porto and I. Z. Rothstein, Phys. Rev. D **78**, 044012 (2008).
[54] R. A. Porto, Classical Quantum Gravity **27**, 205001 (2010).
[55] R. A. Porto, A. Ross, and I. Z. Rothstein, J. Cosmol. Astropart. Phys. 03, (2011) 009.
[56] M. Levi, Phys. Rev. D **82**, 064029 (2010).
[57] M. Levi, Phys. Rev. D **85**, 064043 (2012).
[58] T. Damour and A. Nagar, Phys. Rev. D **76**, 044003 (2007).
[59] T. Damour and A. Gopakumar, Phys. Rev. D **73**, 124006 (2006).
[60] E. Berti, V. Cardoso, and C. M. Will, Phys. Rev. D **73**, 064030 (2006).
[61] W. Tichy and P. Marronetti, Phys. Rev. D **78**, 081501 (2008).
[62] E. Barausse and L. Rezzolla, Astrophys. J. **704**, L40 (2009).
[63] C. Reisswig, S. Husa, L. Rezzolla, E. N. Dorband, D. Pollney *et al.*, Phys. Rev. D **80**, 124026 (2009).
[64] M. Kesden, Phys. Rev. D **78**, 084030 (2008).
[65] C. O. Lousto, M. Campanelli, and Y. Zlochower, Classical Quantum Gravity **27**, 114006 (2010).
[66] R. H. Price and J. Pullin, Phys. Rev. Lett. **72**, 3297 (1994).
[67] M. Davis, R. Ruffini, W. Press, and R. Price, Phys. Rev. Lett. **27**, 1466 (1971).

[68] M. Davis, R. Ruffini, and J. Tiomno, Phys. Rev. D **5**, 2932 (1972).
[69] D. A. Nichols and Y. Chen, Phys. Rev. D **82**, 104020 (2010).
[70] D. A. Nichols and Y. Chen, Phys. Rev. D **85**, 044035 (2012).
[71] J. M. Bardeen, W. H. Press, and S. A. Teukolsky, Astrophys. J. **178**, 347 (1972).
[72] L. Barack and N. Sago, Phys. Rev. Lett. **102**, 191101 (2009).
[73] A. Le Tiec, E. Barausse, and A. Buonanno, Phys. Rev. Lett. **108**, 131103 (2011).
[74] D. McKechan, C. Robinson, and B. Sathyaprakash, Classical Quantum Gravity **27**, 084020 (2010).
[75] The numerical relativity and analytical relativity (NRAR) collaboration, https://www.ninja-project.org/doku.php?id=nrar:home.
[76] L. S. Collaboration, LSC Algorithm Library software packages lal, lalwrapper, and lalapps, http://www.lsc-group.phys.uwm.edu/lal.
[77] T. Damour, Phys. Rev. D **81**, 024017 (2010).
[78] L. Barack, T. Damour, and N. Sago, Phys. Rev. D **82**, 084036 (2010).
[79] A. Le Tiec, L. Blanchet, and B. F. Whiting, Phys. Rev. D **85**, 064039 (2012).
[80] E. Barausse, A. Buonanno, and A. Le Tiec, Phys. Rev. D **85**, 064010 (2012).